E-21-F17

REPORT

TO THE

NATIONAL AERONAUTICS AND SPACE ADMINISTRATION

- AMES RESEARCH CENTER -

FINAL TECHNICAL REPORT

(INCLUDES QUARTERLY REPORT #9)

for

GRANT NAG 2-515

PIONEER-VENUS RADIO
OCCULTATION (ORO) DATA REDUCTION:
PROFILES OF 13 CM ABSORPTIVITY

Paul G. Steffes, Principal Investigator

July 1, 1988 through September 30, 1990

Submitted by

Professor Paul G. Steffes
School of Electrical Engineering
Georgia Institute of Technology
Atlanta, Georgia 30332-0250
(404) 894-3128

TABLE OF CONTENTS

I. Introduction

Recent studies of the radio emission spectrum of Venus [Steffes, 1986 and Steffes et al., 1990] have suggested that variations (both temporal and spatial) in the abundances of sulfur-bearing gases may be occurring below the Venus cloud layers. One technique for monitoring the abundances of sulfur-bearing gases (especially gaseous H_2SO_4) is to measure the 13 cm wavelength opacity using Pioneer-Venus Orbiter Radio Occultation studies (PVORO) [Steffes, 1985].

In order to characterize possible variations in the abundance and distribution of subcloud sulfuric acid vapor, we have processed 13 cm radio occultation signals from 23 orbits that occurred in late 1986 and 1987 (Radio Occultation Season #10) and 7 orbits that occured in 1979 (Radio Occultation Season #1). During Season #10, the atmosphere was probed to altitudes as low as 39.4 km (above a mean radius of 6051.92 km) at latitudes in the northern hemisphere from 11 to 89°N. During the orbits from Season #1, the atmosphere was probed to altitudes as low as 36.7 km. The data were inverted to produce 13 cm absorptivity profiles. Finally, pressure and temperature profiles obtained with the Pioneer-Venus night probe and the northern probe [Seiff et al., 1980] were used along with the absorptivity profiles to infer upper limits for vertical profiles of the abundance of gaseous H_2SO_4. In addition to inverting the data, error bars have been placed on the absorptivity profiles and H_2SO_4 abundance profiles using the standard propagation of errors [Brandt, 1963]. These error bars were developed by considering the effects of statistical errors only. The profiles show a distinct pattern with regard to latitude which is consistent with latitude variations observed in data obtained during occultation seasons #1 and #2 (late 1978 and early 1979) [Cimino, 1982]. However, when compared with the earlier data, the recent occultation studies suggest that the amount of sulfuric acid vapor occurring at and below the main cloud layer may have decreased during the time interval between early 1979 and late 1986.

II. Processing of Radio Occultation Data

Radio occultation studies using the Pioneer-Venus Orbiter allow us greater flexibility in studying the vertical structure of the neutral atmosphere of Venus than either in-situ probes or radio astronomical observations. The atmosphere can be probed at a wide range of latitudes due to the geometry of the spacecraft's orbit and its changing orientation with respect to Earth throughout an occultation season. In addition, the longevity of the orbiter has made it possible to conduct long term studies of the microwave properties of the atmosphere of Venus with greater vertical resolution than radio astronomical observations.

Complete descriptions of the theoretical bases for this technique are given in Fjeldbo and Eshleman (1965), Fjeldbo et al. (1971) and Eshleman (1973). For the Pioneer-Venus application, consider the geometry illustrated by Figure 1. In this experiment, the spacecraft modulation is switched off and a continuous wave (CW) signal is transmitted during the occultation event. For a successful experiment, the radiated carrier signal must have a stable amplitude and frequency. To ensure that the frequency is stable, a reference signal is uplinked to the spacecraft from the Earth station. The spacecraft locks its oscillator to this signal and downlinks a noninteger harmonic of the received frequency. The power output of the spacecraft is stabilized internally. The occultation experiment begins when the path of the signal transmitted by the spacecraft tangentially grazes the edge of the atmosphere of Venus. As the spacecraft's trajectory carries it toward the limb of the planet, the path of the signal slices deeper into the atmosphere, traversing a longer pathlength through the limb. Refraction in the atmosphere causes the signal to bend around the limb of the planet. This increases the Doppler shift since a larger component of the velocity of the spacecraft is now parallel to the ray path back to Earth. It is important to note that this also affects the uplinked reference signal from Earth. Hence the Doppler shift of the signal received at Earth includes the shift incurred by the uplink to the spacecraft as well as by the downlink.

The power of the received signal is attenuated by two atmospheric effects and by mispointing of the spacecraft antenna. The curvature of the atmosphere and the changing refractive index profile cause spreading of the transmitted beam, an effect known as refractive defocusing. Secondly, absorption and scattering in the atmosphere extract energy from the signal, causing an additional drop in received power. In addition, as the ray is bent by refraction in the atmosphere, it is also bent away from the main axis of the spacecraft antenna, causing a drop in power due to the smaller off-axis gain of the antenna. As the experiment progresses, the Doppler shift increases and the amplitude drops until the spacecraft can no longer maintain lock with the uplinked frequency reference.

For Figure 1, we assume that for each instant in time, the illustrated distances R_e, D and y (and hence, R_{es}, R_s and the angle γ are known from interpolations of spacecraft tracking data, from Earth and planetary ephemerides and from the knowledge of the tracking station position relative to the center of the Earth. Thus the other quantities follow as:

$$\begin{aligned} a &= D\sin(\delta-\beta) + y\cos(\delta-\beta) \\ \delta &= (\delta-\beta) + \sin^{-1}(a/R_e) \\ R_1 &= (R_e^2-a^2)^{1/2} \\ R_2 &= (R_s^2-a^2)^{1/2} \end{aligned} \tag{1}$$

[Eshleman et al., 1980].

The impact parameter a and the bending angle δ can be used to calculate the vertical profile of refractivity if we assume a perfectly stratified atmosphere with no horizontal variations other than planetary curvature in the region probed by the beam [Fjeldbo et al., 1971]:

$$\ln(n(r)) = \frac{1}{\pi}\int_{a(r)}^{\infty} \frac{\delta(a)\,da}{\sqrt{a^2-a^2(r)}} \tag{2}$$

The lowest depth, r, probed for each ray is related to the ray impact parameter by a = n·r. Thus, the natural log of the index of refraction n is the inverse Abel transform of the integral of the bending angle δ. Once n(r) is determined it is possible to obtain pressure and temperature profiles, assuming hydrostatic equilibrium and that the major constituents are well known and well mixed [Lipa and Tyler, 1979].

In order to invert the amplitude data to obtain absorptivity profiles it is necessary to first remove the effects of refractive defocusing and mispointing of the spacecraft antenna. The refractive defocusing can be computed using geometric optics and is then subtracted from the signal attenuation profile. Let I be the received signal intensity normalized by the free space intensity at the spacecraft receiver input. Then the reduction in intensity due to refractive defocusing, I^{-1}, is given by

$$I^{-1} = \left(\frac{y}{R_{es}\sin\beta}\right)\left(\frac{\cos(\delta-\beta)\,dy}{R_{es}\,d\beta}\right) \tag{3}$$

where the first bracketed term represents the focusing effect of the curved limb normal to the plane of the figure and the second term is the refractive defocusing in the plane of the figure [Eshleman et al., 1980]. For an Earth-Venus distance much larger than the spacecraft-Venus distance, equation (3) reduces to

$$I^{-1} = \frac{y}{a(1-R_2\frac{d\beta}{da})} \tag{4}$$

[Eshleman et al., 1980].

To understand the importance of the antenna pointing issue, it must be noted that, as currently operated, the direction of the beam of the High Gain Antenna (HGA) aboard the Pioneer-Venus Orbiter is only adjusted once per orbit so that it is pointed directly to Earth at the periapsis of each orbit. Since the ray path back to Earth can be bent by as much as 3.5° from the true direction to Earth, significant signal reductions occur. These reductions are not due to atmospheric effects, but are due to the gain dependence of the orbiter antenna on incidence angle. During the Pioneer-Venus primary mission, slew commands were sent to the orbiter so that the antenna beam would continually track the virtual image of the Earth. Thus, little if any correction was needed for power variation due to S-band antenna mispointing. However, since such tracking was not used during Season #10, it is necessary to trace the ray path for each data point and determine the gain of the orbiter antenna at the ray's angle of departure.

After correcting the amplitude data for the effects of refractive defocusing and for antenna mispointing, we are left with the excess attenuation profile τ. This residual attenuation is the result of integrating the absorption coefficient α over the downlink ray path for each sample point. (This assumes that scattering is negligible compared to absorption at the transmitted frequency.) This can be written as an integral over radius using Bouger's rule [Lipa and Tyler, 1979]:

$$\tau(r_0) = 2\int_{r_0}^{\infty} \frac{\alpha(r)\,dr}{\sqrt{1-\left(\frac{a(r_0)}{r\cdot n(r)}\right)^2}} \qquad (5)$$

where τ is in dB and α is expressed in dB/km. This expression can be rewritten in the form of an Abel transform by making the approximation da ≈ n·dr:

$$\tau(r_0) = 2\int_{r_0}^{\infty} \frac{\alpha(r(a))}{n(r(a))} \cdot \frac{a\,da}{\sqrt{a^2-a(r_0)^2}} \qquad (6)$$

The form of the Inverse Abel Transform that has been applied to the data is the following:

$$\alpha(r_0) = -\frac{n(r_0)}{2\pi a(r_0)} \cdot \frac{d}{da}\left[2\int_{a(r_0)}^{\infty} \frac{\tau(a)\,a\,da}{\sqrt{a^2-a(r_0)^2}}\right] \qquad (7)$$

Thus, the absorption coefficient can be recovered as a function of height by applying an inverse Abel transform to the excess attenuation τ and multiplying the result by the refractivity profile.

Although this is a fairly complete description of the mathematical procedure for reducing radio occultation data, a complete analysis requires characterization of experimental uncertainties. Since the derived quantities α and n cannot be observed directly, neither can the uncertainties associated with each of them. The next section describes our method for placing error bars on the absorptivity profiles.

III. Error Analysis

Statistical errors are inherent in any set of experimental observations. The significance of small scale structure in experimental data is dependent on the magnitude of these statistical errors. Thus, knowledge of the variance of the noise fluctuations riding on the true data is necessary to evaluate the validity of theoretical predictions or to compare independent sets of observations. In the case of indirect observations, where the desired vector quantity, y, is obtained by transforming the observed vector of quantities, x, it is not possible to measure the noise power directly. If y is related to x by a linear transform T_{yx}, then the covariance matrix of y is given by

$$C_y = T_{yx} C_x T_{yx}^T \tag{8}$$

where

$$C_x = \langle (x-\hat{x}) \cdot (x-\hat{x})^T \rangle \tag{9}$$

[Brandt, 1963]. Here, x is the vector of true values, and $\hat{x}$ is the measured, or average value and $\langle \cdot \rangle$ is the expectation operator. If the errors are small and the transform T_{yx} is nonlinear, then C_y can be estimated by expanding T_{yx} in a Taylor series

$$y = t_0 + T_1 (x-\hat{x}) + T_2 (x-\hat{x})^2 + \ldots \tag{10}$$

where

$$T_1 = \begin{bmatrix} \frac{\partial y_1}{\partial x_1}\Big|_{x=\hat{x}} & \frac{\partial y_1}{\partial x_2}\Big|_{x=\hat{x}} & \cdots & \frac{\partial y_1}{\partial x_n}\Big|_{x=\hat{x}} \\ \frac{\partial y_2}{\partial x_1}\Big|_{x=\hat{x}} & \frac{\partial y_2}{\partial x_2}\Big|_{x=\hat{x}} & \cdots & \frac{\partial y_2}{\partial x_n}\Big|_{x=\hat{x}} \\ \vdots & \vdots & & \vdots \\ \frac{\partial y_m}{\partial x_1}\Big|_{x=\hat{x}} & \frac{\partial y_m}{\partial x_2}\Big|_{x=\hat{x}} & \cdots & \frac{\partial y_m}{\partial x_n}\Big|_{x=\hat{x}} \end{bmatrix} \qquad (11)$$

Now the estimate for the C_y is given by

$$C_y = T_1 \cdot C_x \cdot T_1^T \qquad (12)$$

This is the result of neglecting all terms higher than first order and is known as the standard propagation of errors [Brandt, 1963].

To see how this method may be applied to a multistep procedure such as the reduction of radio occultation data, consider the vector quantity $z = T_2 y$. Now, C_z is given by

$$\begin{aligned} C_z &= T_2 C_y T_2^T \\ &= T_2 (T_1 C_x T_1^T) T_2^T \\ &= (T_2 T_1) C_x (T_2 T_1)^T \\ &= T_3 C_x T_3^T \end{aligned} \qquad (13)$$

where $T_3 = T_2 T_1$. This forms the basis for placing error bars on the absorptivity profiles discussed in Section IV. Note that this procedure can be carried out with fewer numerical computations if the sequence of transformation matrices are multiplied in the appropriate order before the covariance matrix for the desired quantity is determined. For example, if k transformations are used which can be represented as n x n matrices, then forming the covariance matrix at each step ($C_i = T_i \cdot C_{i1} \cdot T_i^T$) requires $2n^2$ multiplies for a total of $2kn^2$ operations. By contrast, forming the product $T_f = T_k \cdot T_{k1} \cdot \ldots \cdot T_2 \cdot T_1$ requires kn^2 multiplies and forming the covariance matrix $C = T_f \cdot C_1 \cdot T_f^T$ requires an additional $2n^2$ multiplies, resulting in only $(k+2)n^2$ total operations.

Figure 2 illustrates the propagation of errors through the various steps of inverting the frequency and amplitude data to obtain the absorptivity profile. In the figure, each transformation of variables is represented by a labeled box. The random variables which flow from each box are related to the random quantities that flow into that box by that transform. For example, the ray path parameters are determined from the frequency data and trajectory information. Thus, Δa and $\Delta\delta$ are dependent on the uncertainties in the frequency data, Δf. In the first step, errors are estimated for power and frequency. Lipa and Tyler (1979) developed a model for estimating these errors based on their method for estimating the amplitude and frequency of the sampled signal received from the spacecraft. In the case of this study, the available data consisted only of the excess Doppler shift (Hz) and relative power (dB) as time series. Because the original sampled signal is needed to estimate the errors in frequency and power by Lipa and Tyler's method, an alternative method has been developed.

The approach used is to fit a line to the set of points $\{f(t_{n-4}), f(t_{n-3}), \ldots, f(t_{n-1}), f(t_n), f(t_{n+1}), \ldots, f(t_{n+3}), f(t_{n+4})\}$ for each point t_n in time, and use the mean square error as the estimate for Δf_n, the variance for the frequency at point n. The same procedure is used to estimate the variance at each point of the power profile. Since the noise process is very nearly white Gaussian noise and is stationary over short intervals [Lipa and Tyler, 1979], this provides a simple method for estimating the errors Δf and Δp. We are assuming (as did Lipa and Tyler) that the random processes Δf and Δp are independent and uncorrelated so that $<p_m \cdot f_n> = 0$ for all m and n, and $<p_m \cdot p_n> = <f_m \cdot f_n> = 0$ for $m \neq n$. Thus the covariance matrices C_f and C_p are diagonal and the covariance matrix C_{fp} is identically zero.

The next step involves determining the uncertainties in the ray path parameters, which are derived from the frequency data and the spacecraft trajectory. The equations used to determine these parameters are linearized and the standard propagation of errors used so that

$$\begin{aligned} C_\delta &= T_{\delta f} C_f T_{\delta f}^T \\ C_a &= T_{af} C_f T_{af}^T \\ C_{\delta a} &= T_{\delta f} C_f T_{af}^T = C_{a\delta}^T \end{aligned} \tag{14}$$

Since C_f is diagonal, C_δ, $C_{\delta a}$ and C_a are also diagonal at this point of the processing. This assumes that the uncertainties in the trajectory data are negligible compared to the uncertainties arising from the noise on the received signal.

Before the index of refraction is calculated, all profiles, such as a, δ, and p are "averaged and decimated" by partitioning the points of each profile into bins based on ray asymptote height.

The size of the bins is specified by the user and, in most cases in this study, is 0.5 km. The points in each bin are replaced by a single point which is the average value of all the points in that bin. This is a useful technique since the derivative $d\delta/da$ increases as the occultation progresses, causing the points to become denser in altitude with respect to time. The result is a set of vectors which have been decreased from a typical length of over 400 to less than 100 points. An additional benefit is that the variance of each new point is roughly a factor of $1/n$ times the variances of the n points in that bin. Also,the points at the bottom of each profile, which are more noisy than upper points, have experienced more averaging, and hence, greater reduction in noise, due to the fact that the lower bins tend to have more points in them.

Because of this significant reduction in the lengths of all the vectors used in the remaining data reduction, it is convenient to trace the errors as they propagate through the data processing by considering the transformations of the vectors δ, a and p. Thus, all references to the covariance matrices associated with these vectors, C_δ, C_a, or C_p, or the uncertainties $\Delta\delta$, Δa or Δp are with regard to this stage of the processing.

The uncertainties associated with the index of refraction is determined as per Lipa and Tyler (1979). The exponential function imbedded in equation (2) is approximated by linearizing about zero, the integral is approximated by a summation using the trapezoidal rule and the result is linearized with respect to the variables δ

and a so that

$$\Delta n = T_{n\delta}\Delta\delta + T_{na}\Delta a \tag{15}$$

where $T_{n\delta}$ is the linear transform relating δ to n (to the first order), and T_{na} is the transform relating a to n.

From the fact $a = n \cdot r$, it follows that

$$\begin{aligned} \Delta r &= T_{ra}\Delta a + T_{rn}\Delta n \\ &= (T_{ra} + T_{rn}T_{na})\Delta a + T_{rn}T_{n\delta}\Delta\delta \end{aligned} \tag{16}$$

where T_{ra} is a diagonal matrix with diagonal entries $(T_{ra})_{ii} = n_i^{-1}$ and T_{rn} is a diagonal matrix with diagonal entries $(T_{rn})_{ii} = -a_i/n_i^2$.

After the calculation of the index of refraction, all vectors are averaged and decimated again, only this time with respect to the radius profile instead of the ray asymptote. Then, if desired, the data is smoothed by a 5 point running average. Let T_{ave} denote the matrix representing the process of averaging and decimating the vectors, and T_s denote the matrix representing the smoothing process.

Now the excess attenuation is determined by performing the antenna correction and removing the refractive defocusing. We have determined that the uncertainties in performing the antenna correction are small compared to the other sources of error (by 3 orders of magnitude) and have chosen to neglect them. We have

$$\Delta\tau = T_{\tau p}\Delta p + T_{\tau a}T_s T_{ave}\Delta a + T_{\tau\delta}T_s T_{ave}\Delta\delta \tag{17}$$

where $T_{\tau a}$ and $T_{\tau\delta}$ are due to refractive defocusing.

The inverse Abel transform of the excess attenuation is computed in two steps. Examining equation (7) reveals that the integral corresponds to the forward Abel transform of τ. The result of this transform is arbitrarily named F and has the associated uncertainty

$$\begin{aligned}\Delta F &= T_{F\tau}\Delta\tau + T_{Fa}\Delta a \\ &= T_{F\tau}T_{\tau p}\Delta p + T_{F\tau}T_{\tau\delta}T_{s}T_{ave}\Delta\delta \\ &\quad + (T_{F\tau}T_{\tau a}T_{s}T_{ave} + T_{Fa})\Delta a \\ &= T'_{Fp}\Delta p + T'_{F\delta}\Delta\delta + T'_{Fa}\Delta a\end{aligned} \qquad (18)$$

The derivative of F is taken with respect to a and scaled by the factor $-n/(2\pi a)$ to yield the absorptivity profile α. The uncertainty in α is given by

$$\begin{aligned}\Delta\alpha &= T_{\alpha F}\Delta F + T_{\alpha a}\Delta a + T_{\alpha n}\Delta n \\ &= T_{\alpha F}(T'_{Fp}\Delta p + T'_{F\delta}\Delta\delta + T'_{Fa}\Delta a) \\ &\quad + T_{\alpha a}\Delta a + T_{\alpha n}(T_{n\delta}\Delta\delta + T_{na}\Delta a) \\ &= T_{\alpha F}T'_{Fp}\Delta p + (T_{\alpha F}T'_{F\delta} + T_{\alpha n}T_{n\delta})\Delta\delta \\ &\quad + (T_{\alpha F}T'_{Fa} + T_{\alpha a} + T_{\alpha n}T_{na})\Delta a \\ &= T'_{\alpha p}\Delta p + T'_{\alpha\delta}\Delta\delta + T'_{\alpha a}\Delta a\end{aligned} \qquad (19)$$

Finally, it is possible to compute the covariance matrix of α:

$$
\begin{aligned}
C_\alpha &= \langle \Delta\alpha \cdot \Delta\alpha^T \rangle \\
&= T'_{\alpha p} C_p T'^T_{\alpha p} + T'_{\alpha\delta} C_\delta T'^T_{\alpha\delta} + T'_{\alpha a} C_a T'^T_{\alpha a} \qquad (20) \\
&\quad + T'_{\alpha\delta} C_{\delta a} T'^T_{\alpha a} + T'_{\alpha a} C_{a\delta} T'^T_{\alpha\delta}
\end{aligned}
$$

Since $C_{\delta a} = C_{a\delta}^T$, we need only compute one of the final two terms in the sum above. The error bars displayed on the figures discussed in the next section are the square roots of the diagonal elements of the matrix C_α.

IV. Discussion of Results

Table I lists the 23 data sets from Season #10 (July 23, 1986 through January 7,1987) and the 7 data sets from Season #1 (December 28, 1978 through January 26, 1979) which have been reduced by the method described in section II. The latitude and solar zenith angles for the deepest point probed in each experiment are given, as well as the maximum absorptivity measured before loss of lock (in the case of the entry occultations). Most of the occultations were entries and are denoted by the suffix "N". Orbit 2787X is the only data set analyzed which resulted from an exit occultation. We found that the data sets from most exit occultation experiments had to be discarded due to the instability of the spacecraft's onboard oscillator. Although the frequency data from 2787X appears to be relatively stable (in that the data could be processed), the results for this experiment are not deemed to be as reliable as the data from the entry occultations.

Figures 3 through 5 show the absorptivity measured for entry occultation experiments conducted for orbits 2787, 2801 and 2928, respectively. Figures 6 through 10 show averages of the 13 cm absorptivity profiles we have currently obtained for 5 different latitudinal areas, based on the 23 profiles currently available. Figure 6 is the result of averaging profiles 2787N and 2792N. Figure 7 is the result of combining 2798N and 2801N. The profile in Figure 8 is the result of averaging 2814N, 2815N, 2819N, 2859N, 2860N, 2862N and 2952N. Profiles 2844N, 2845N, 2850N, 2851N and 2853N were combined to produce Figure 9. Figure 10 is the result of averaging 2921N, 2923N, 2928N and 2930N. Profiles 2939N and 2955N were not included in the averaged profiles of Figures 9 and 8, respectively, due to the relatively high altitude at which loss of signal occurred in these experiments. Profile 2787N was not included due to the unknown systematic errors resulting from the unstable spacecraft frequency for exit occultations.

When the occultation profiles for the different areas are compared, it appears that the level of significant absorptivity for the various latitudinal regions decreases with increasing latitude. A similar effect had been observed with the 1979 data, although the difference between the levels for the polar occultations and the collar occultations (latitudes in the 70°s) was severe. Since the 13 cm opacity is principally due to gaseous H_2SO_4 [Steffes, 1985], this suggests a variation in the altitude of the cloud base with latitude (i.e. the altitude below which the absorption occurs). Although, the error bars are quite large (there is no statistically significant absorptivity in many of the profiles), we view the trends in the latitudinal variations as being valid. This is especially noticeable in Figure 11, where the average absorptivity profile for the equatorial zone is compared with that for polar latitudes.

Moreover, when these absorption profiles (and the values for peak absorptivities below the clouds, as shown in Table I) are compared with those obtained during the initial Pioneer-Venus radio occultations (1978-79) [Cimino, 1982], it appears that the average 13 cm opacity has dropped, implying a reduced abundance of sulfuric acid vapor. While this is suggestive of long-term temporal variation in the subcloud abundance of gaseous H_2SO_4, it cannot be considered proof until the uncertainties in the earlier absorptivity profiles are properly characterized. We have newly processed 7 orbits from Radio Occultation Season #1 (including error bars). An example of these profiles is shown in Figure 12 (Orbit 40N). The larger significant absorptivity is noteworthy, especially when compared with the average for the 70° latitude range obtained during Season #10 (Figure 9). An average of orbits from Season #1 at latitudes above 70°N (24N, 40N and 44N) is given in Figure 13, along with the averaged profile for 70° obtained for Season #10. This figure suggests graphically that the abundance of H_2SO_4 decreased from 1979 to 1986, although the error bars for both profiles do overlap somewhat.

Figure 14 through 36 display the abundance of sulfuric acid vapor as a function of radius inferred from the derived absorptivity profiles from all 23 orbits analyzed from Season #10 and the saturation vapor pressure using results from a recent laboratory measurement by Fahd and Steffes (1990). For Figures 14 through 18, the pressure and temperature measurements from the Pioneer-Venus night probe were used to derive the abundance profiles. The pressure and temperature measurements from the Pioneer-Venus north probe were used for Figures 19 through 36 [Seiff, et al., 1980]. These figures show the extent to which interpretation of the amplitude data from occultation experiments can be carried, that is, to determine upper limits for the concentration of opaque constituents in planetary atmospheres.

V. Summary of Activities

In the 27 months of Grant NAG 2-515 (July 1, 1988 through September 30, 1990) we have worked on reducing 13 cm radio occultation data to obtain 13 cm absorptivity profiles and the resulting abundance profiles for gaseous H_2SO_4. A summary of our activities is given in Table II. During this period of time all previously existing software was corrected and modified to apply the standard propagation of errors to each step in the processing of the data to derive error bars for the absorptivity profiles and H_2SO_4 abundance profiles. This activity has been conducted using the JPL-Radio Occultation Data Analysis Network (JPL-RODAN), which was accessed remotely from Georgia Tech both by telephone modem and by INTERNET/ARPANET. We worked with JPL to improve the function of its INTERNET interface. This allowed us to off-load some data processing and data analysis to Georgia Tech machines. Graduate student Jon M. Jenkins and Professor Steffes visited JPL 5 times during the course of the project to load the data sets from magnetic tape and process them with the new error estimating software. Also, we attended 5 Pioneer-Venus Science Steering Group (PV-SSG) meetings and have worked effectively with the Radio Science Team Leader (Dr. A. J. Kliore) to evaluate the data.

In May 1990, we submitted a paper to the journal Icarus entitled, "Results for 13 cm Absorptivity and H_2SO_4 Abundance Profiles from the Season 10 (1986) Pioneer-Venus Radio Occultation Experiment" [Jenkins and Steffes, 1990]. In this paper, we described our work in developing 13 cm absorptivity profiles and their accompanying error bars for the orbits listed in Table I. (Note that the 13 cm abundance profiles are directly related to the abundances of gaseous H_2SO_4, as discussed previously.)

V. Conclusions and Suggestions for Future Work

As noted, the error bars placed on the absorptivity profiles derived using the current method are quite large. This may be due in part to overestimating the uncertainties in the frequency and power profiles at the beginning of the process. However, we feel that it is better to overestimate the errors rather than to underestimate them. It is clear that the final step of transforming the excess attenuation into absorptivity via the inverse Abel transform introduces the greatest statistical errors into the measurements. This is due to the fact that the inverse Abel transform corresponds to half order differentiation

[Bracewell, 1977]. Thus, it may be possible to reduce the magnitude of the estimated errors and retain small-scale structure by employing an alternative method for evaluating this recalcitrant transform.

In order to accomplish this task, software is being developed to simulate the occultation experiment. Given a model atmosphere and spacecraft trajectory, the software will generate time series for the received power and frequency. Noise will be added to these quantities and the results fed to the data inversion software. By inserting various methods for computing the inverse Abel transform into the inversion software, their performances can be objectively compared to select the method which is most stable and accurate under low signal-to-noise conditions. This simulation software will not only allow us to determine the method which best handles noise, but will also allow us to locate and evaluate some sources of systematic errors within the data inversion software. Graduate Assistant Jon M. Jenkins will continue to pursue this in his dissertation research. His Ph.D. Thesis (expected 6/91) will include both the Venus atmospheric results described here and the new techniques for processing radio occultation data.

The Pioneer-Venus Orbiter Radio Occultation experiments represent a potentially powerful tool for examining the middle atmosphere of Venus. Our results suggest the presence of latitudinally-dependent variations in the abundance of sulfuric acid vapor and a global decrease in the overall abundance of H_2SO_4 below the main cloud layer. In the future, we hope to be able to verify the statistical validity of these possibilities by modifying the techniques applied in the data inversion software and reprocessing additional data from earlier occultation seasons. Likewise, we hope that radio occultation opportunities using the more powerful Magellan spacecraft can be used to probe to deeper altitudes with higher accuracies than have been previously achieved.

VII. BIBLIOGRAPHY

Bracewell, R. N. (1977). The Fourier Transform and Its Applications, 2nd ed., McGraw-Hill, New York, 244-250.

Brandt, S. (1963). Statistical and Computational Methods in Data Analysis. North-Holland, Amsterdam.

Cimino, J. B. (1982). The composition, vertical structure, and global variability of the lower cloud deck on Venus as determined by radio occultation techniques. Ph.D. Thesis, California Institute of Technology, Pasadena.

Eshleman, V. R. (1973). The radio occultation method for the study of planetary atmospheres. Planetary Space Science **21**, 1521-1531.

Eshleman, V. R., D. O. Muhleman, P. D. Nicholson and P. G. Steffes (1980). Comment on absorbing regions in the atmosphere of Venus as measured by radio occultations. Icarus **44**, 793-803.

Fahd, A. K. and Steffes, P. G. (1990). Laboratory measurements of the vapor pressure of gaseous sulfuric acid (H_2SO_4) under simulated conditions for the Venus atmosphere. To be submitted to Icarus.

Fjeldbo, G. and V. R. Eshleman (1965). Scientific Report No. 5, NSF G-377, SU-SEL-65-010, Stanford Electronics Laboratories, Stanford University, Stanford, California.

Fjeldbo, G., A. J. Kliore and V. R. Eshleman (1971). The neutral atmosphere of Venus as studied with the Mariner V radio occultation experiments. Astronomical Journal **76**, No. 2, 123-140.

Hoffman, J. H., R. R. Hodges, Jr., M. B. McElroy, T. M. Donahue and M. Kolpin (1979). Composition and structure of the Venus atmosphere: Results from Pioneer Venus. Science **205**, 49-52.

Jenkins, J. M. and Steffes, P. G. (1990). Results for 13 cm absorptivity and H_2SO_4 abundance profiles from the season #10 (1986) Pioneer-Venus Orbiter radio occultation experiment. Submitted to Icarus.

Lipa, B. and G. L. Tyler (1980). Statistical and computational uncertainties in atmospheric profiles from radio occultation: Mariner 10 at Venus. Icarus **39**, 192-208.

Seiff, A., D. B. Kirk, R. E. Young, R. C. Blanchard, J. T. Findlay, G. M. Kelly and S. C. Sommer (1980). Measurements of thermal structure and thermal contrasts in the atmosphere of Venus and related dynamical observations: Results from the four Pioneer Venus probes. Journal of Geophysical Research, Vol. 85, No. A13, 7903-7933, December 30.

Steffes, P. G. (1985). Laboratory measurements of the microwave opacity and vapor pressure of sulfuric acid under simulated conditions for the middle atmosphere of Venus. Icarus **64**, 576-585.

Steffes, P. G. (1986). Evaluation of the microwave spectrum of Venus in the 1.2 to 22 centimeter wavelength range based on laboratory measurements of constituent gas opacities. Astrophysical Journal **310**, 482-489, November 1, 1986.

Steffes, P. G., Klein, M. J. and Jenkins, J. M. (1990). Observations of the microwave emission of Venus from 1.3 to 3.6 cm. Icarus **84**, 83-92.

TABLE I. DATA SUMMARY

Orbit*	Latitude (°)	S Z A (°)	Depth** (km)	Maximum Absorptivity Measured Before Loss of Signal (dB/km)
Season 10:				
2787N	11.1	160.6	47.0	0.0095 ± 0.0035
2787X	-37.7	139.9	44.4	0.010 ± 0.001
2792N	24.8	151.7	45.9	0.010 ± 0.0045
2798N	36.1	142.1	43.7	0.0085 ± 0.009
2801N	40.8	137.7	42.0	0.0031 ± 0.0028
2814N	59.3	118.6	41.3	0.0036 ± 0.0039
2815N	60.7	117.2	40.6	0.0044 ± 0.0045
2819N	65.6	111.6	40.2	0.0030 ± 0.0049
2844N	79.6	79.1	40.9	0.0054 ± 0.0051
2845N	79.3	78.4	41.7	0.0027 ± 0.0055
2850N	75.6	73.5	41.9	0.004 ± 0.005
2851N	74.4	72.2	41.5	0.0034 ± 0.0050
2853N	72.6	70.3	41.2	0.005 ± 0.005
2859N	67.3	65.3	40.7	0.0034 ± 0.0051
2860N	66.7	64.8	41.0	0.0066 ± 0.0027
2862N	65.9	64.8	40.7	0.0037 ± 0.0057
2921N	87.2	89.8	40.5	0.0064 ± 0.0050
2923N	88.0	90.9	42.3	0.001 ± 0.007
2928N	88.6	93.8	39.4	0.024 ± 0.010
2930N	87.5	94.6	40.6	0.000 ± 0.002
2939N	77.8	104.0	43.5	0.0082 ± 0.0019
2952N	60.4	121.9	42.0	0.0042 ± 0.0041
2955N	56.4	126.0	43.8	0.0031 ± 0.0029
Season 1:				
24N	87.0	95.0	39.1	0.010 ± 0.001
40N	78.0	104.6	40.9	0.014 ± 0.0014
44N	74.7	107.8	39.9	0.013 ± 0.007
45N	74.1	108.4	43.0	0.0092 ± 0.0019
51N	65.7	116.6	36.7	0.011 ± 0.007
52N	66.0	116.2	39.3	0.0083 ± 0.0017
53N	63.5	118.7	38.0	0.0079 ± 0.0007

* Note that an N suffix indicates an entry occultation, and an X suffix indicates an exit occultation.

** Deepest altitude probed (relative to a radius of 6051.92 km) before loss of signal.

TABLE II

PIONEER-VENUS RADIO OCCULTATION (ORO) DATA REDUCTION: PROFILES OF 13-CM ABSORPTIVITY

FINAL REPORT

1. TO DATE, 23 ORBITS HAVE BEEN PROCESSED FROM OCCULTATION SEASON 10 (LATE 1986 AND EARLY 1987), INCLUDING ERROR BARS AND 7 ORBITS HAVE BEEN PROCESSED FROM OCCULTATION SEASON 1 (EARLY 1979).

2. PROBLEMS IN PREVIOUSLY EXISTING SOFTWARE HAVE BEEN DETECTED IN AREAS OF ANTENNA POINTING CORRECTION, SIGNAL GAIN NORMALIZATION (ALSO KNOWN AS AGC ACTION), AND SIGNAL PATH DETERMINATION. CORRECTIONS HAVE BEEN DEVELOPED.

3. PROFILES OF ABSORPTIVITY AND GASEOUS H_2SO_4 ABUNDANCE AND THE ACCOMPANYING ERROR BARS HAVE BEEN DEVELOPED (2.29 GHz OR 13 cm).

4. PROFILES GENERALLY SHOW A LOWER 13 cm ABSORPTIVITY THAN TYPICALLY MEASURED IN THE FIRST RADIO OCCULTATION SEASON (1979-1980), HOWEVER, PROPER CHARACTERIZATION OF UNCERTAINTIES (I.E. ERROR BARS) OF EARLIER PROFILES IS NECESSARY TO CONFIRM ANY LONG TERM TEMPORAL VARIATION.

5. DATA DOES NOT SUGGEST ANY DIURNAL VARIATIONS TO MATCH THOSE OBSERVED BY EMISION MEASUREMENTS AT 2.6 mm.

6. LATITUDINAL VARIATIONS ARE APPARENT, I.E. ABSORPTIVITY BEGINS AT LOWER ALTITUDES IN POLAR REGIONS.

7. ABUNDANCES OF GASEOUS H_2SO_4 IN THE 5-20 PPM RANGE ARE COMMON BELOW THE CLOUD LAYERS.

8. FUTURE WORK:

   INVESTIGATE ALTERNATIVE METHODS FOR COMPUTING THE INVERSE ABEL TRANSFORM SO AS TO REDUCE UNCERTAINTY IN DERIVED ABSORPTIVITY PROFILES.

   RADIO OCCULTATION STUDIES WITH MORE POWERFUL MAGELLAN SPACECRAFT.

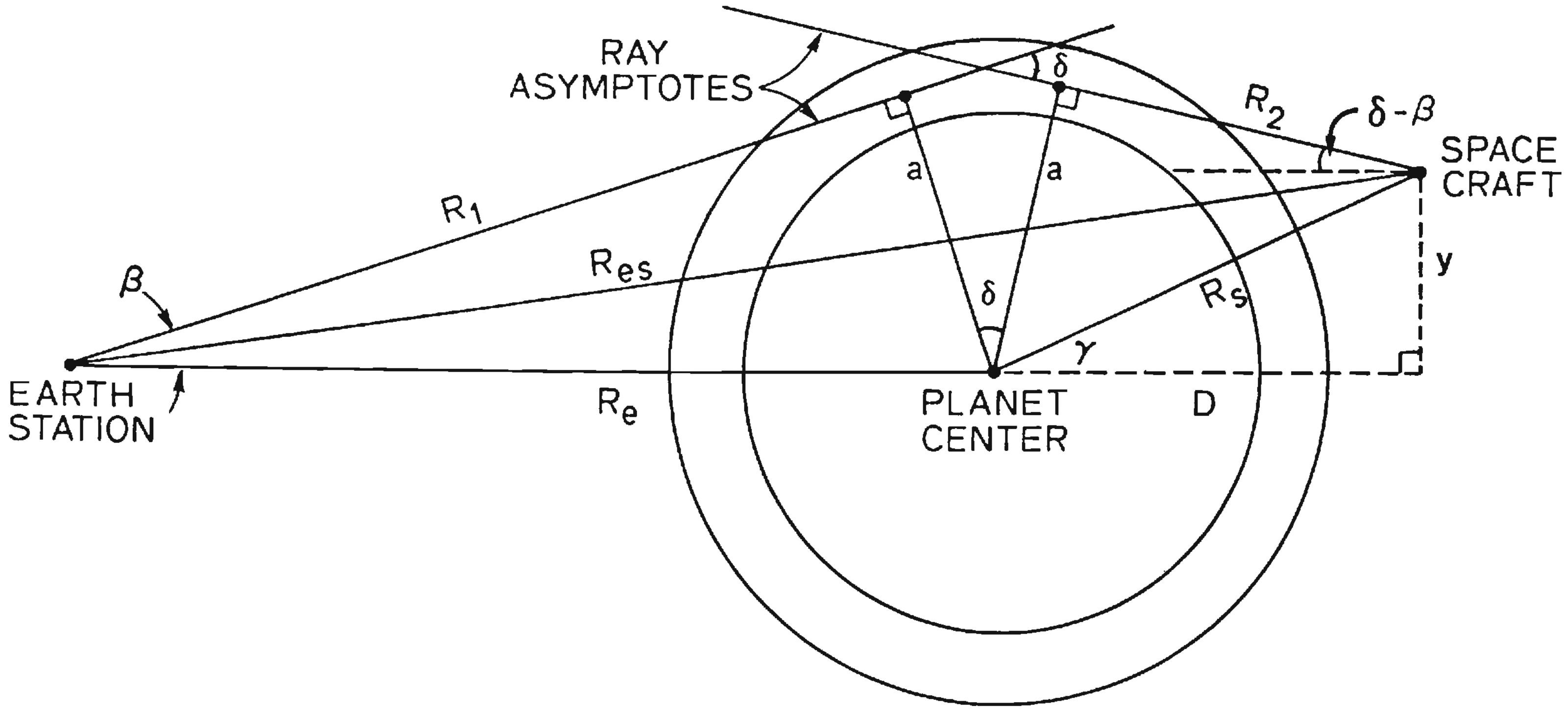

Figure 1: Occultation Geometry

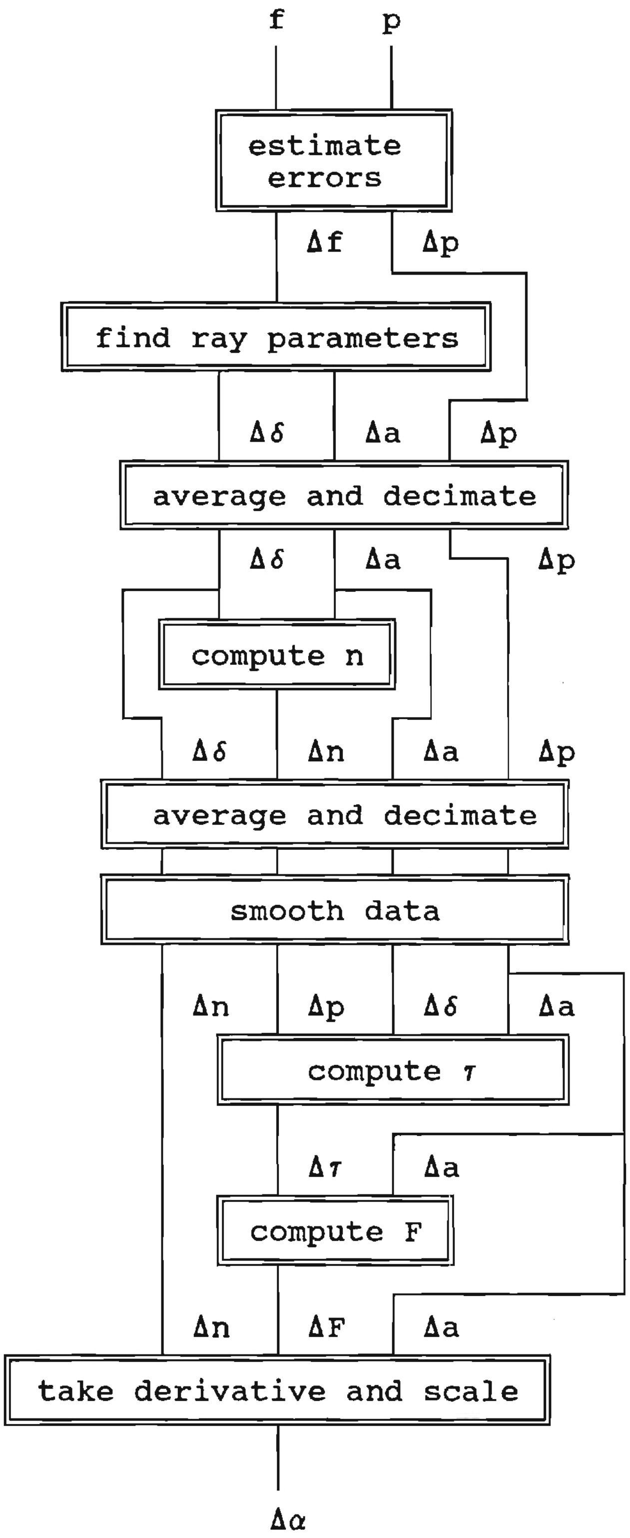

Figure 2: Flow chart for propagation of errors.

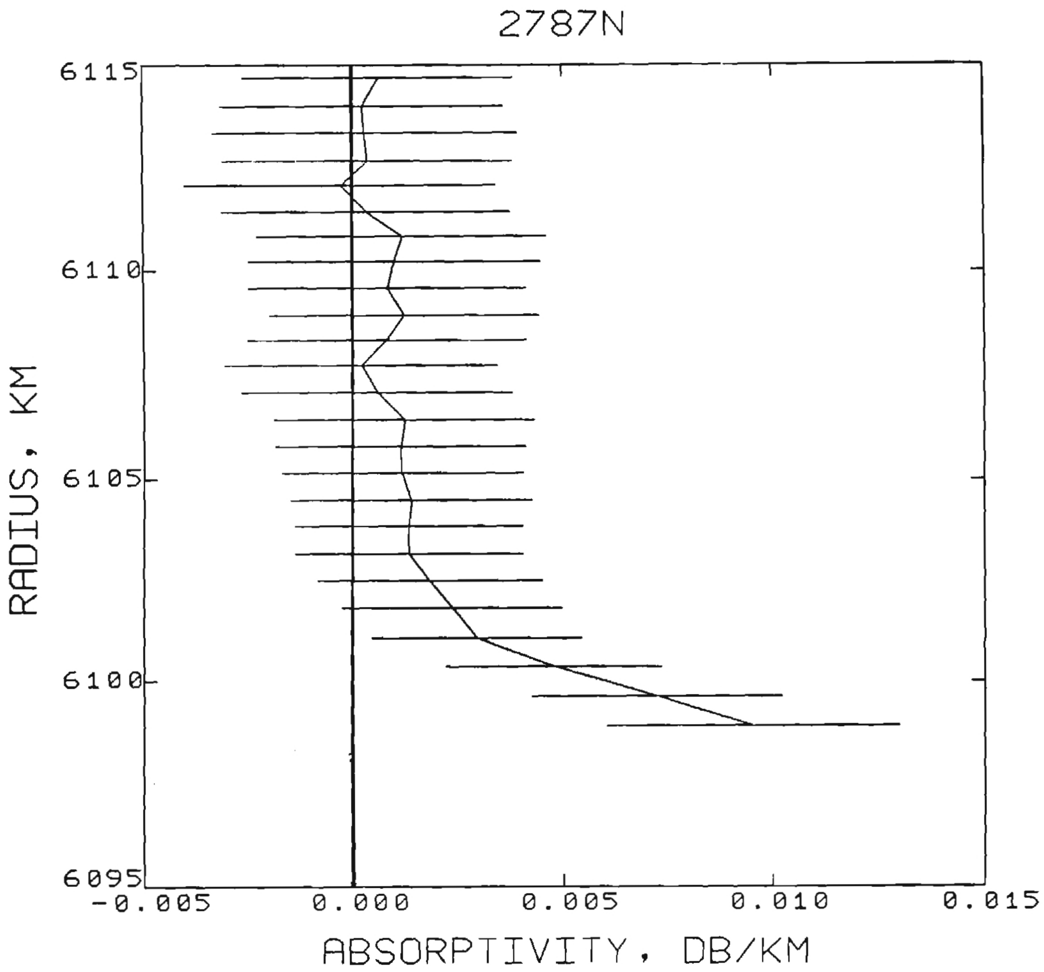

Figure 3: Atmospheric absorptivity profile measured for Orbit 2787N which occurred on July 23, 1986 at 11.1°N.

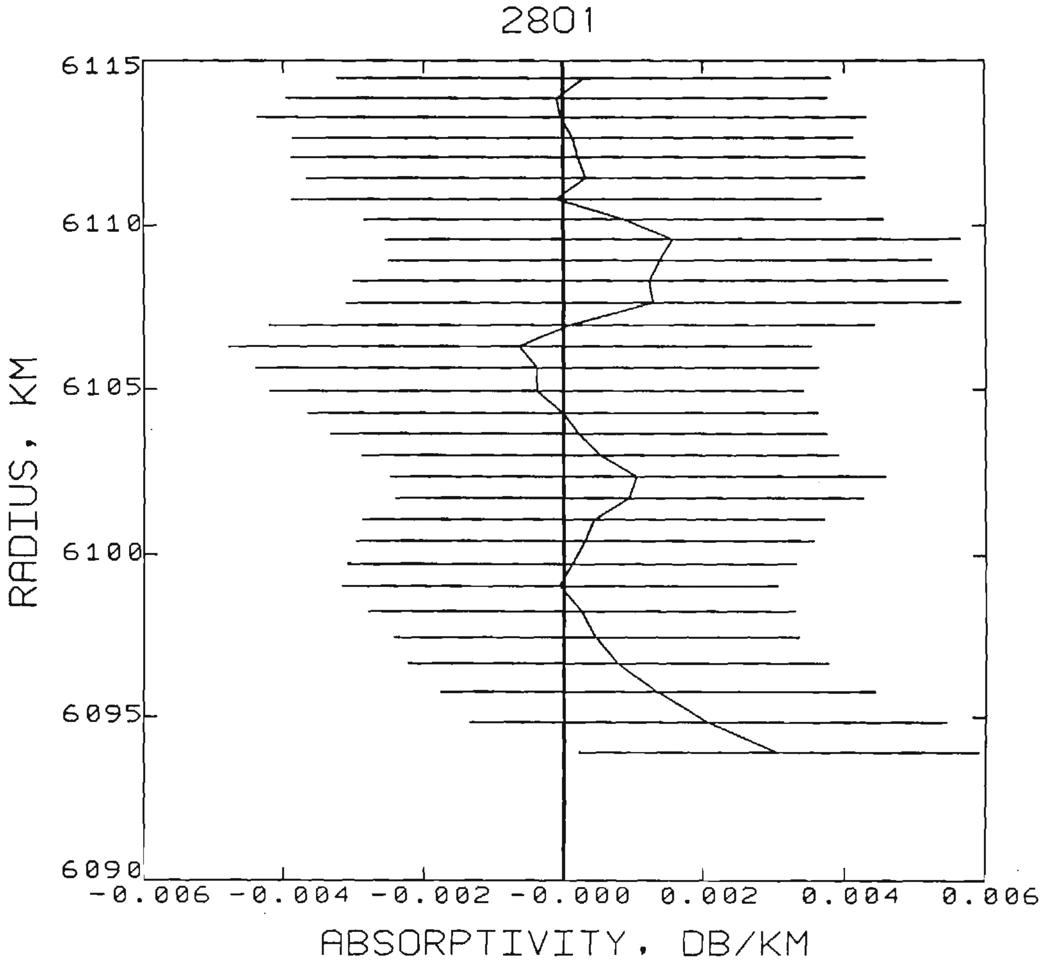

Figure 4: Atmospheric absorptivity profile measured for Orbit 2801N which occurred on August 6, 1986 at 40.8°N.

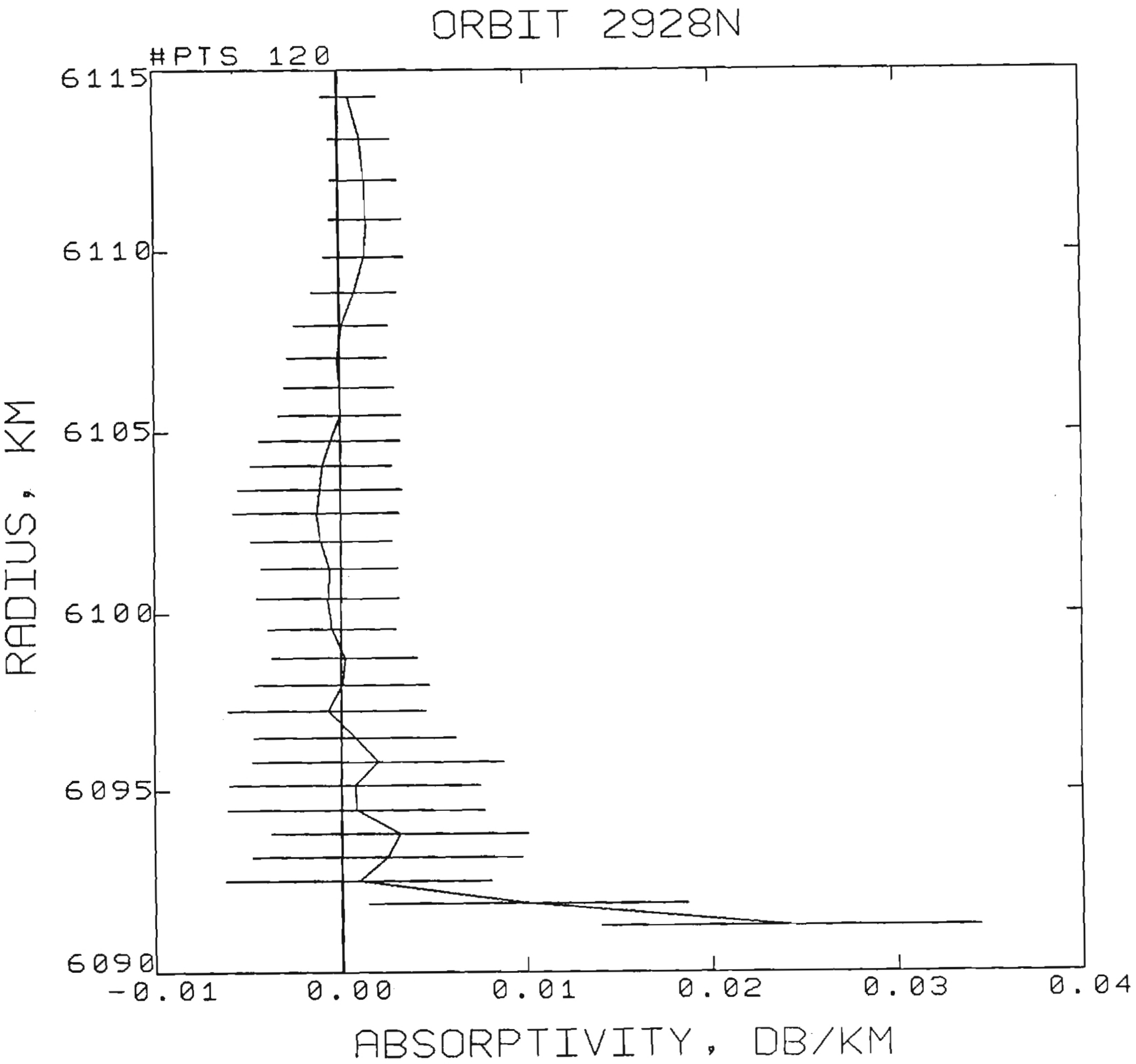

Figure 5: Atmospheric absorptivity profile measured for Orbit 2928N which occurred on December 11, 1986 at 88.6°N.

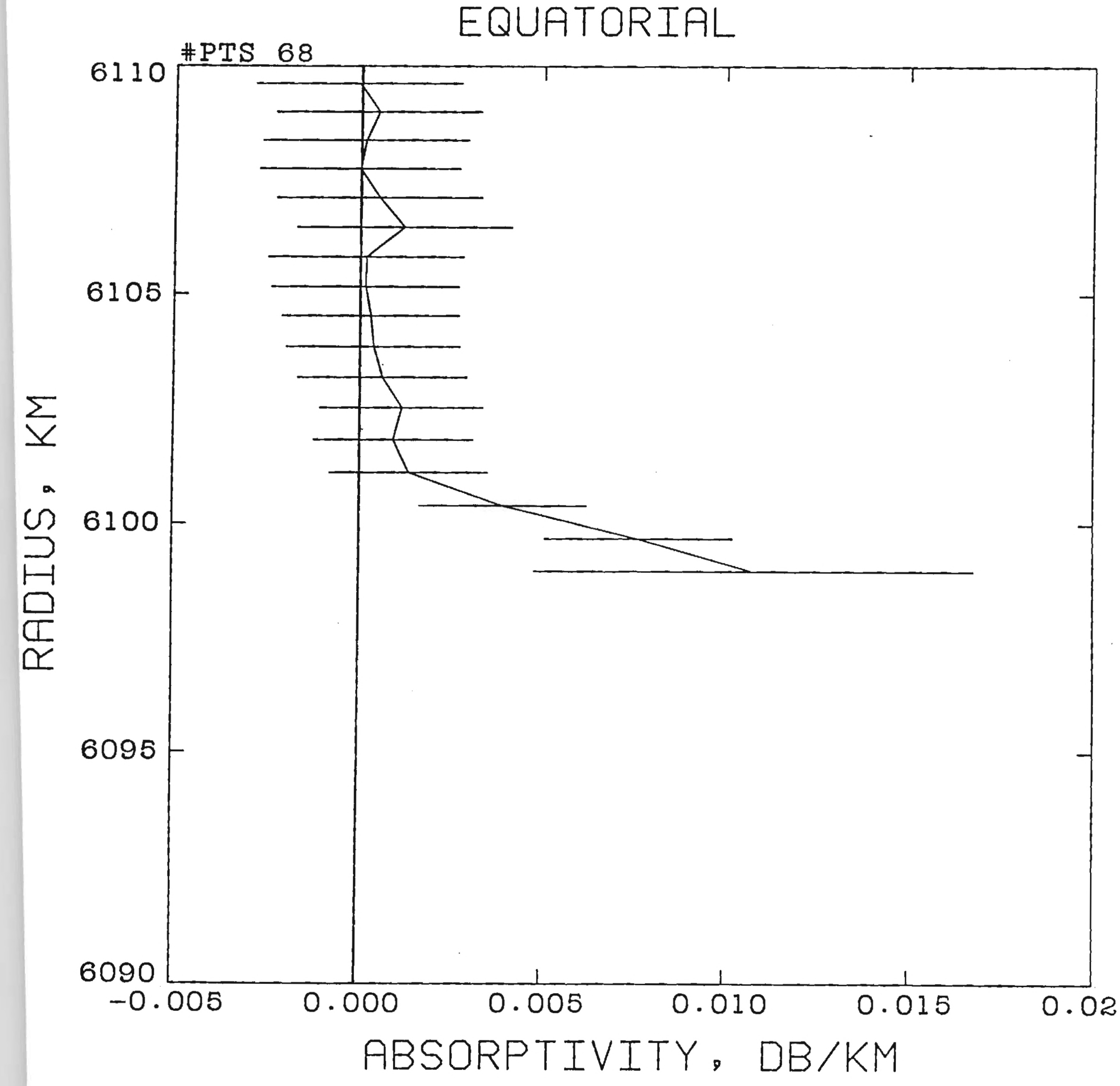

Figure 6: Average 13 cm opacity profile obtained for the equatorial latitudes (11 to 25°N).

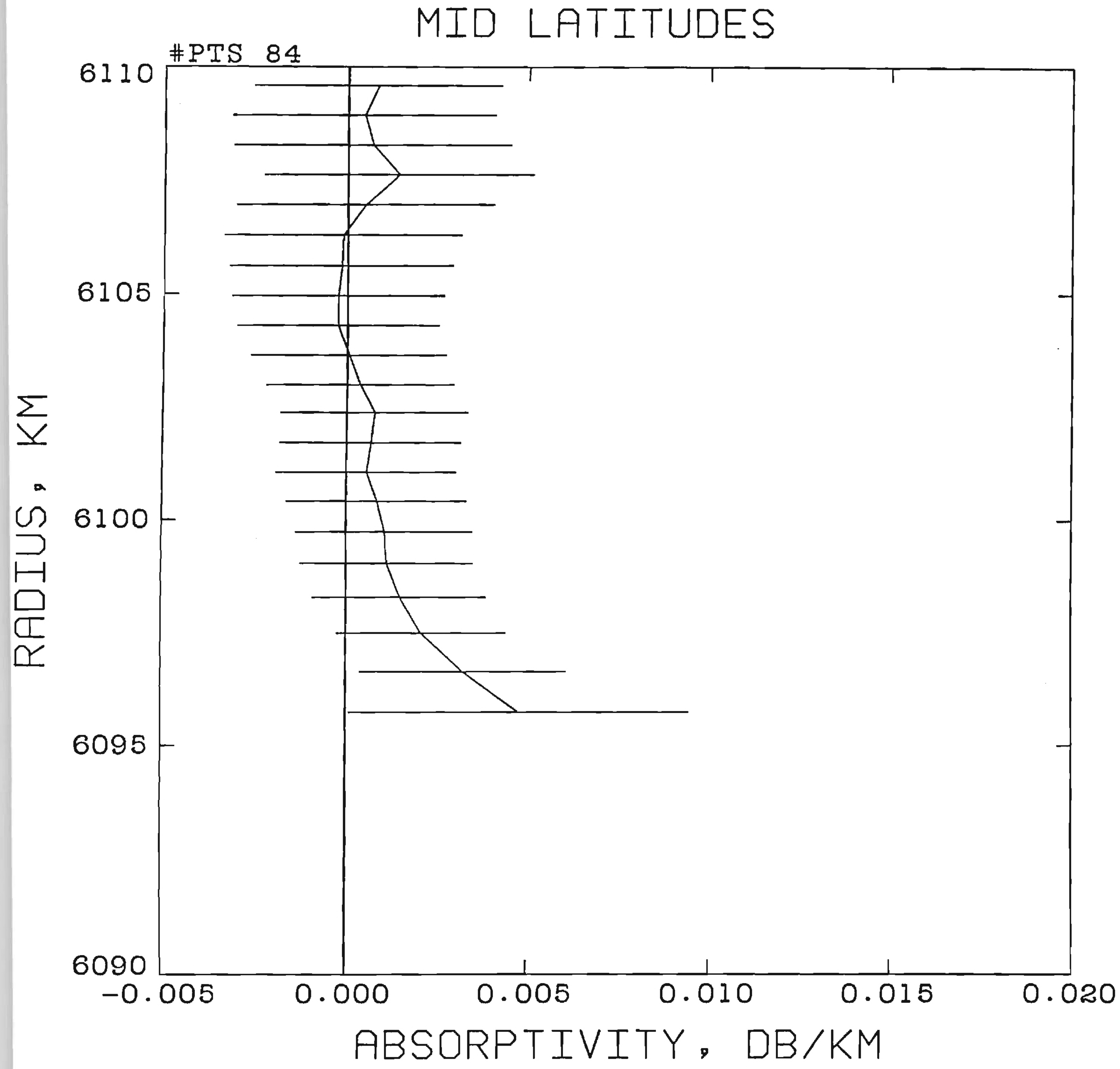

Figure 7: Average 13 cm opacity profile obtained for the mid latitudes (35 to 45°N).

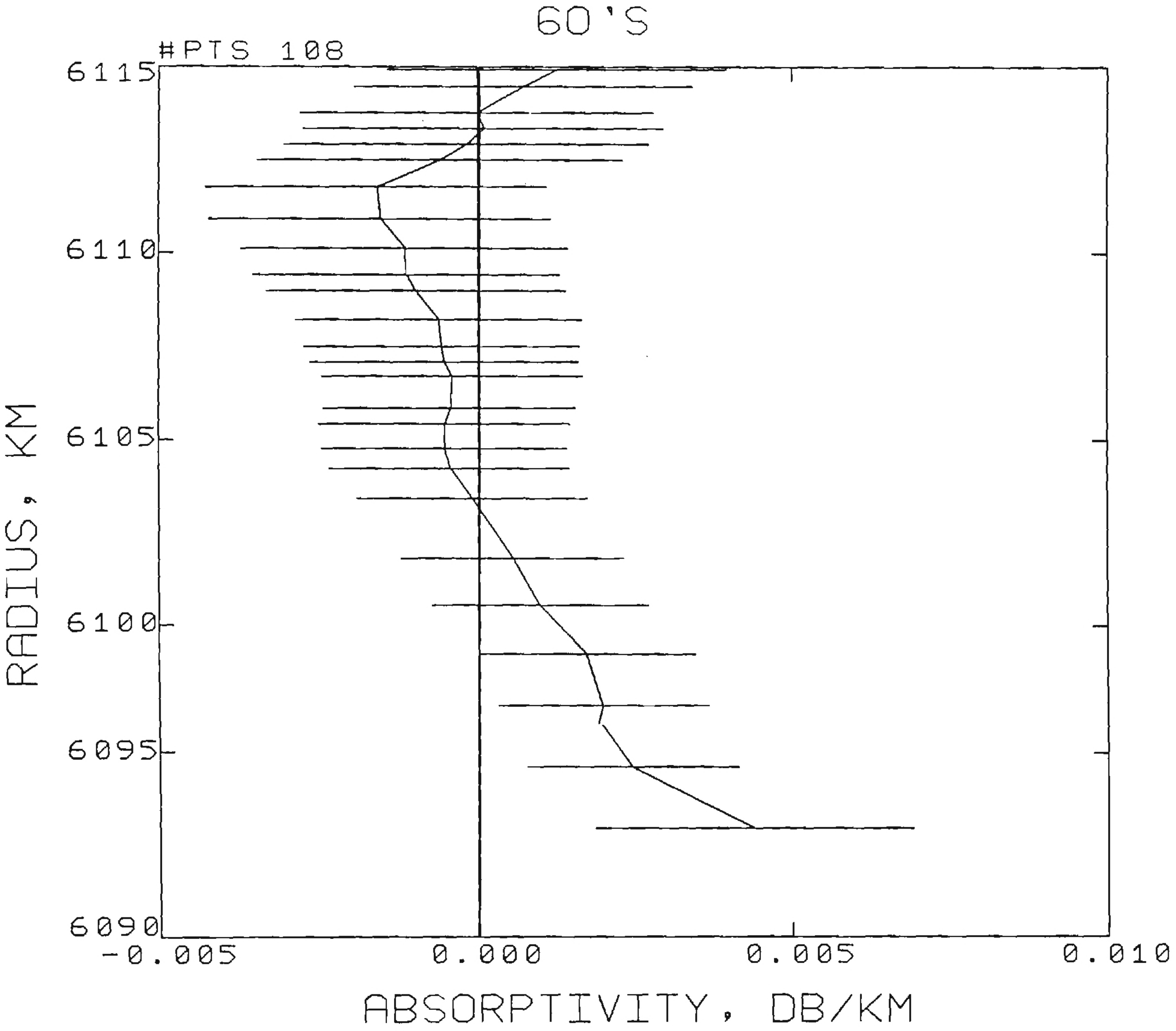

Figure 8: Average 13 cm opacity profile obtained for latitudes between 59 and 68°N.

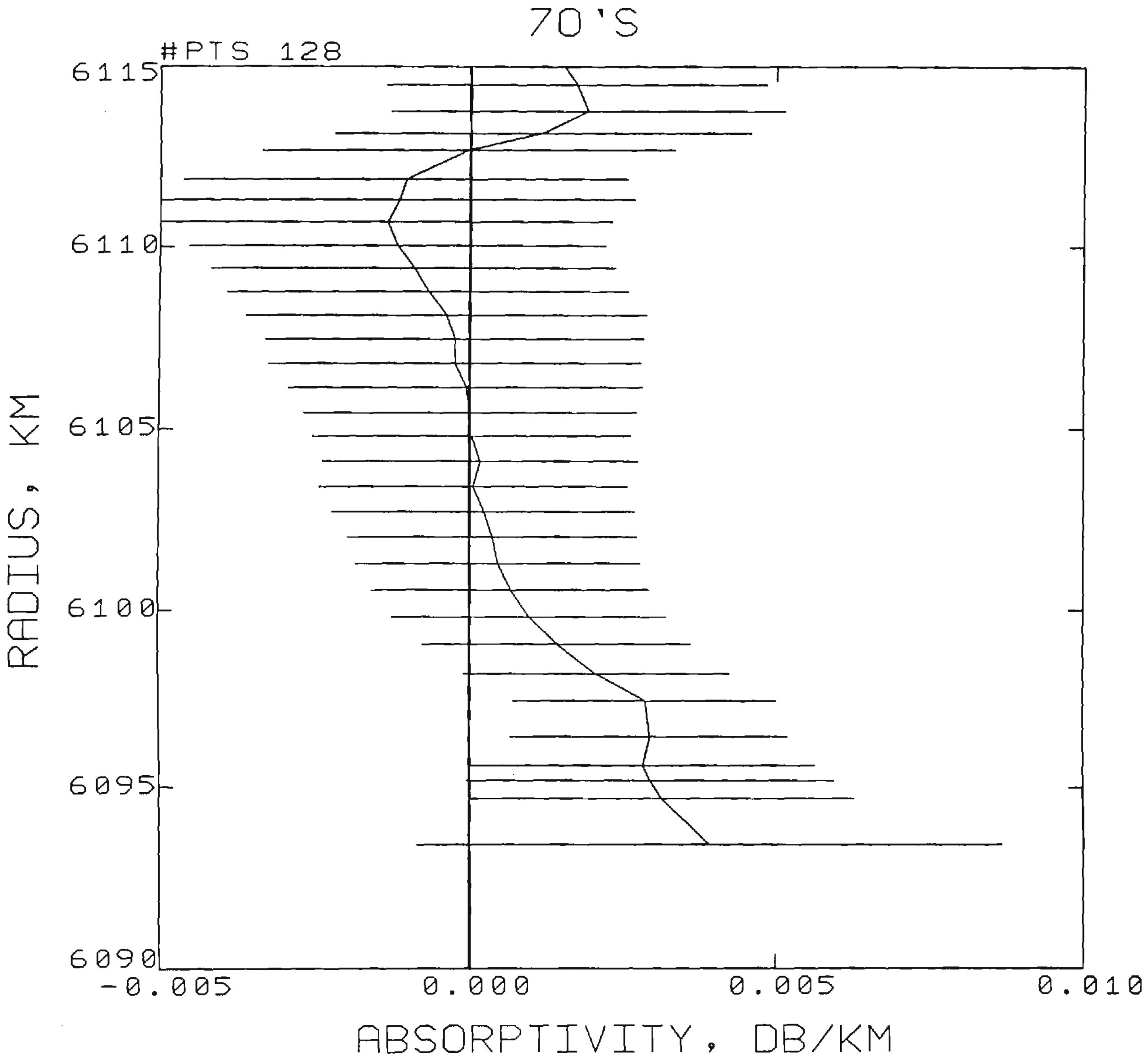

Figure 9: Average 13 cm opacity profile obtained for latitudes between 72 and 80°N.

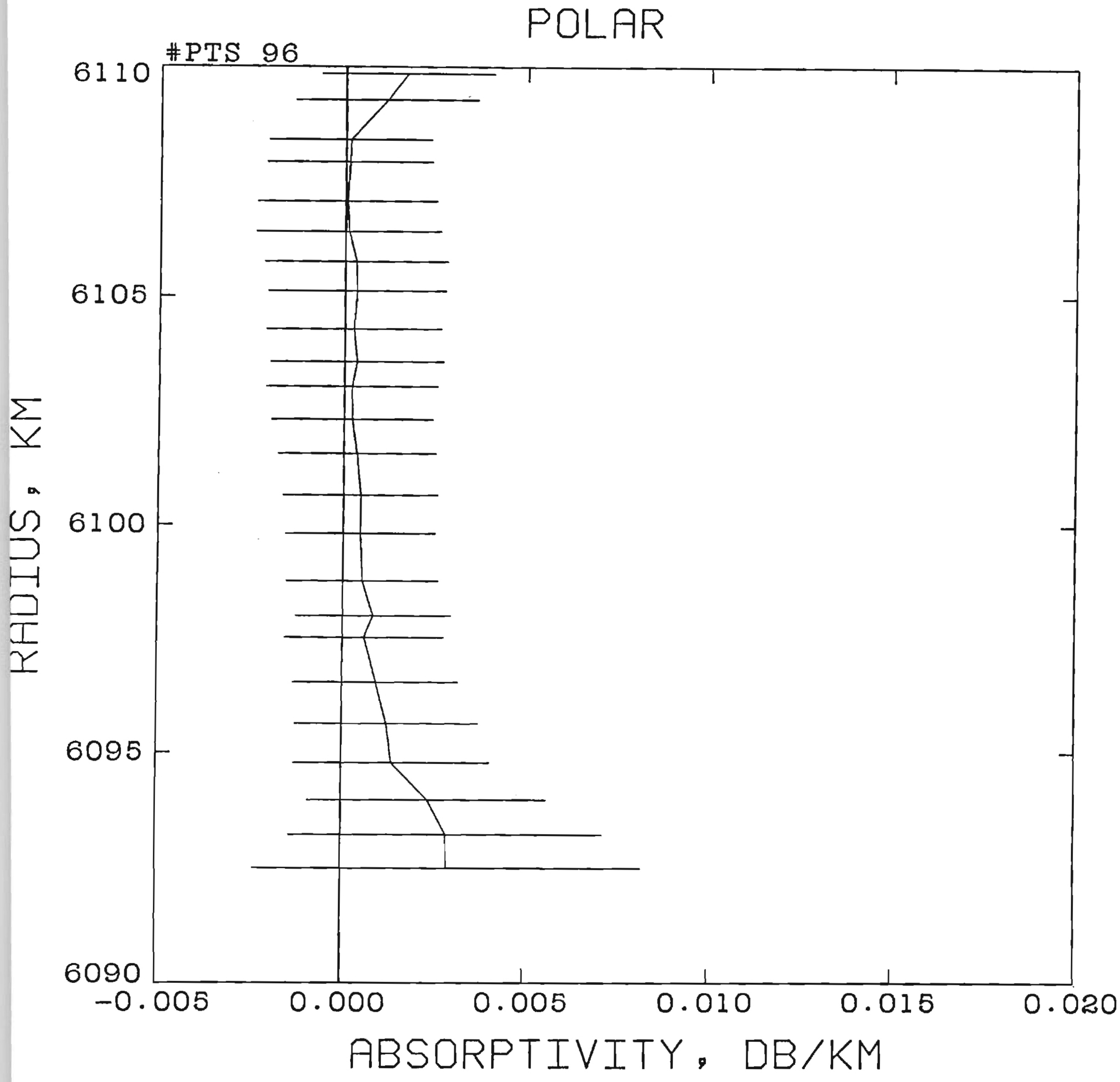

Figure 10: Average 13 cm opacity profile obtained for the polar region (latitudes above 85°N).

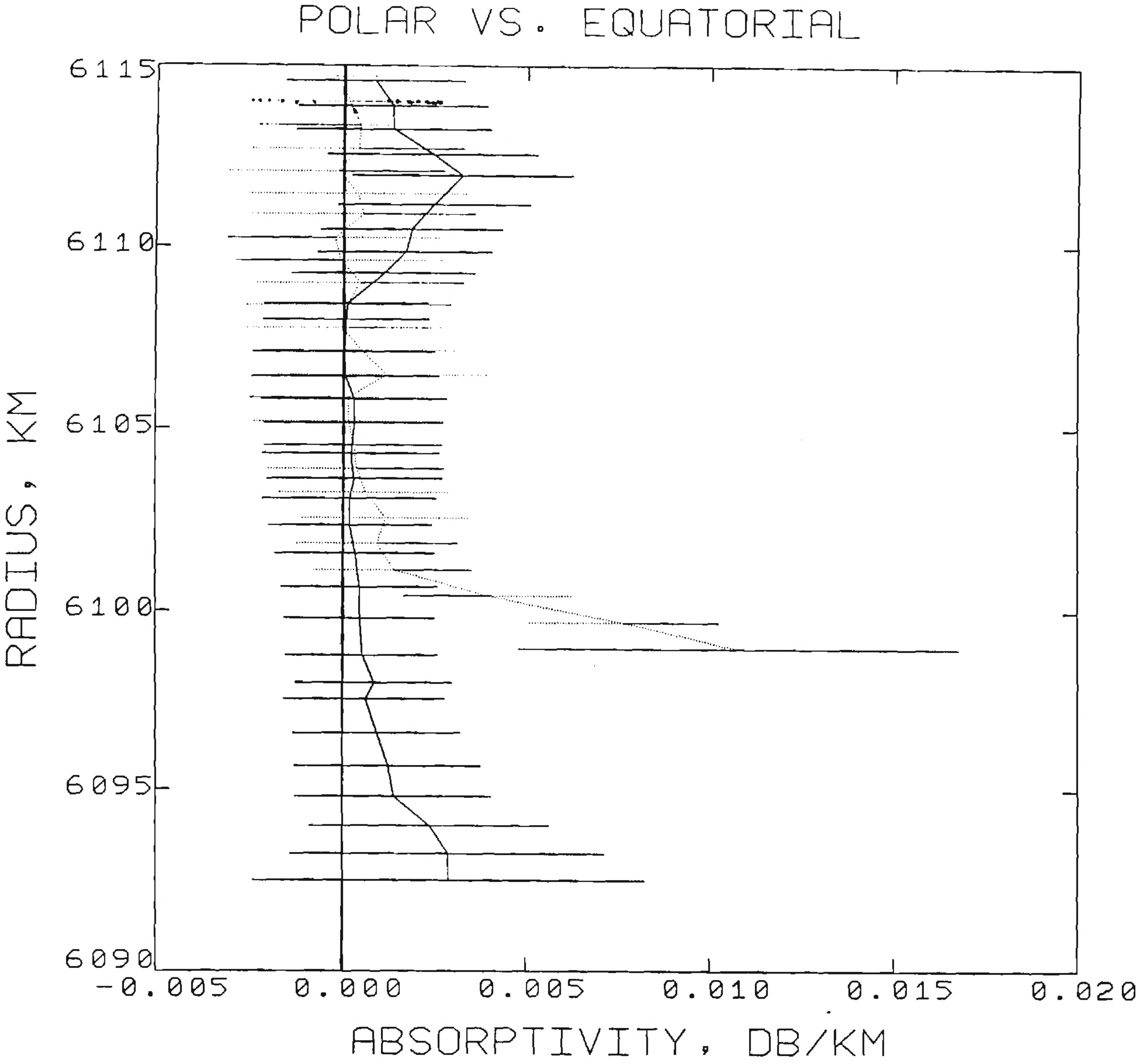

Figure 11: Average 13 cm opacity profiles obtained for the equatorial region (dotted line) and the polar region (solid line).

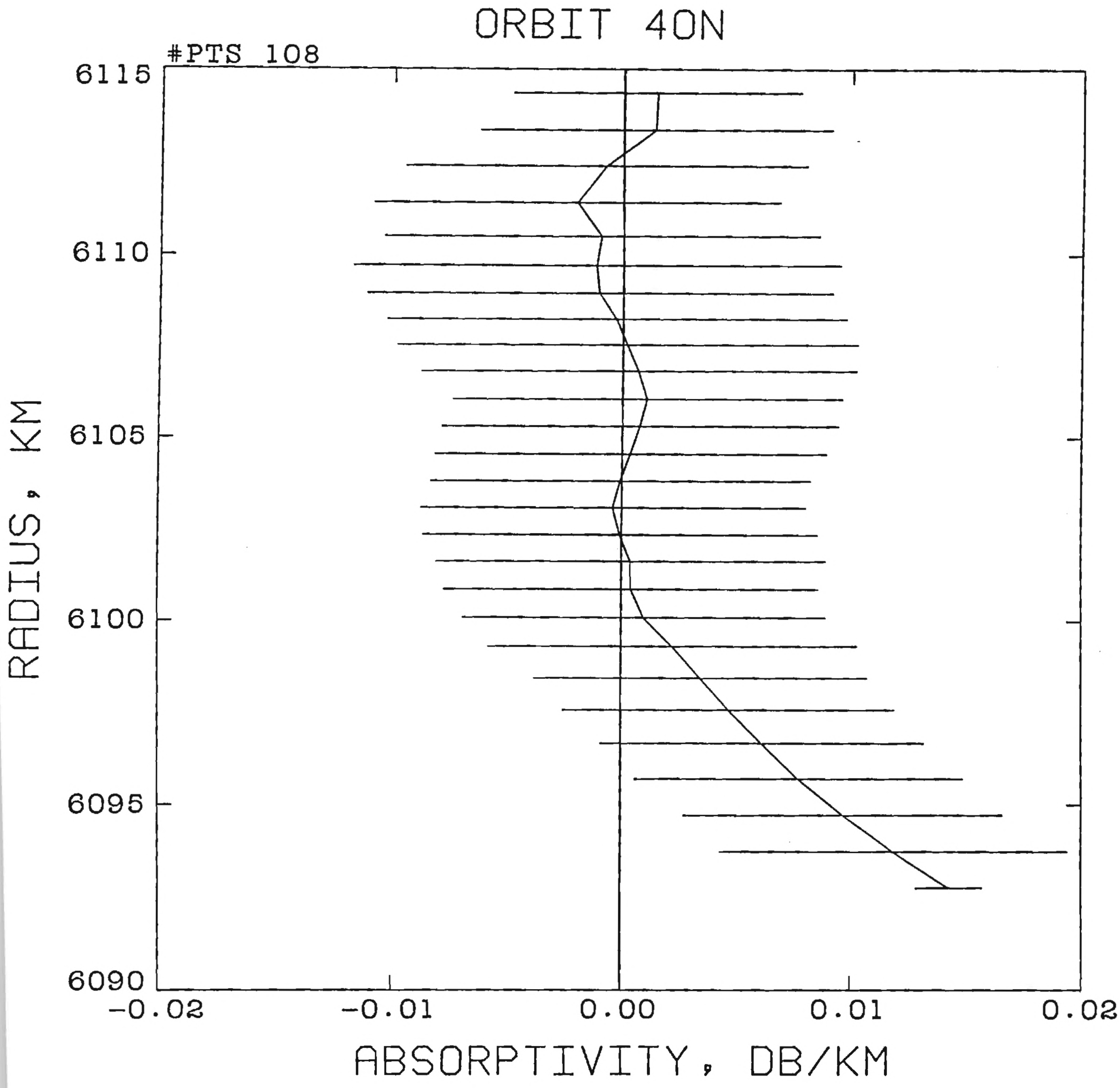

Figure 12: Atmospheric opacity profile measured for Orbit 40N, which occurred on January 13, 1979 at 78°N.

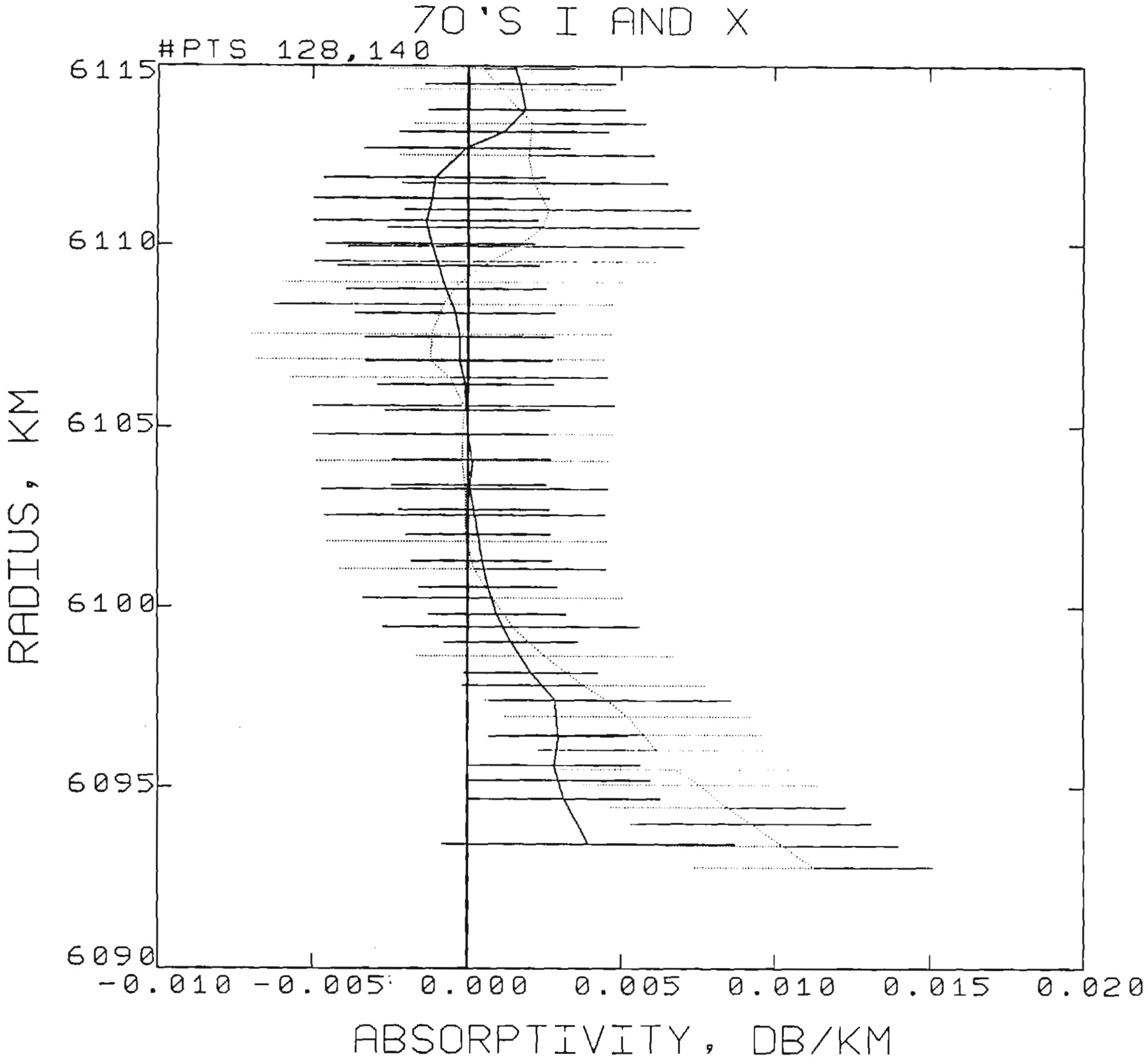

Figure 13: Average 13 cm opacity profiles for latitudes in the 70°s from Season 10 (solid line) and latitudes above 74°N from Season 1.

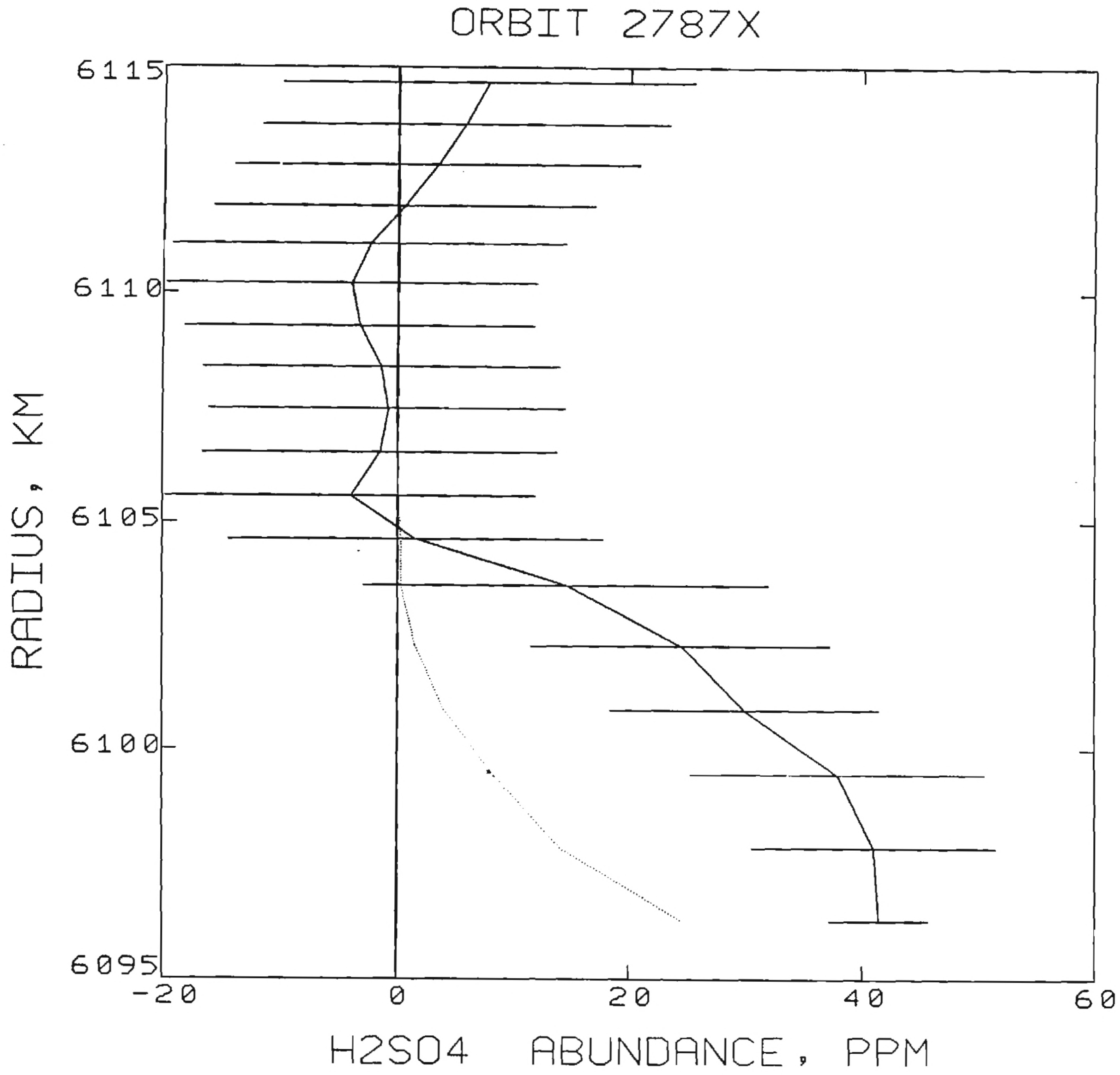

Figure 14: Gaseous H_2So_4 abundance as a function of radius measured for orbit 2787X, which occurred on July 23, 1986 at -37.7°N (solid line) and the abundance expected from saturation vapor pressure (dotted line).

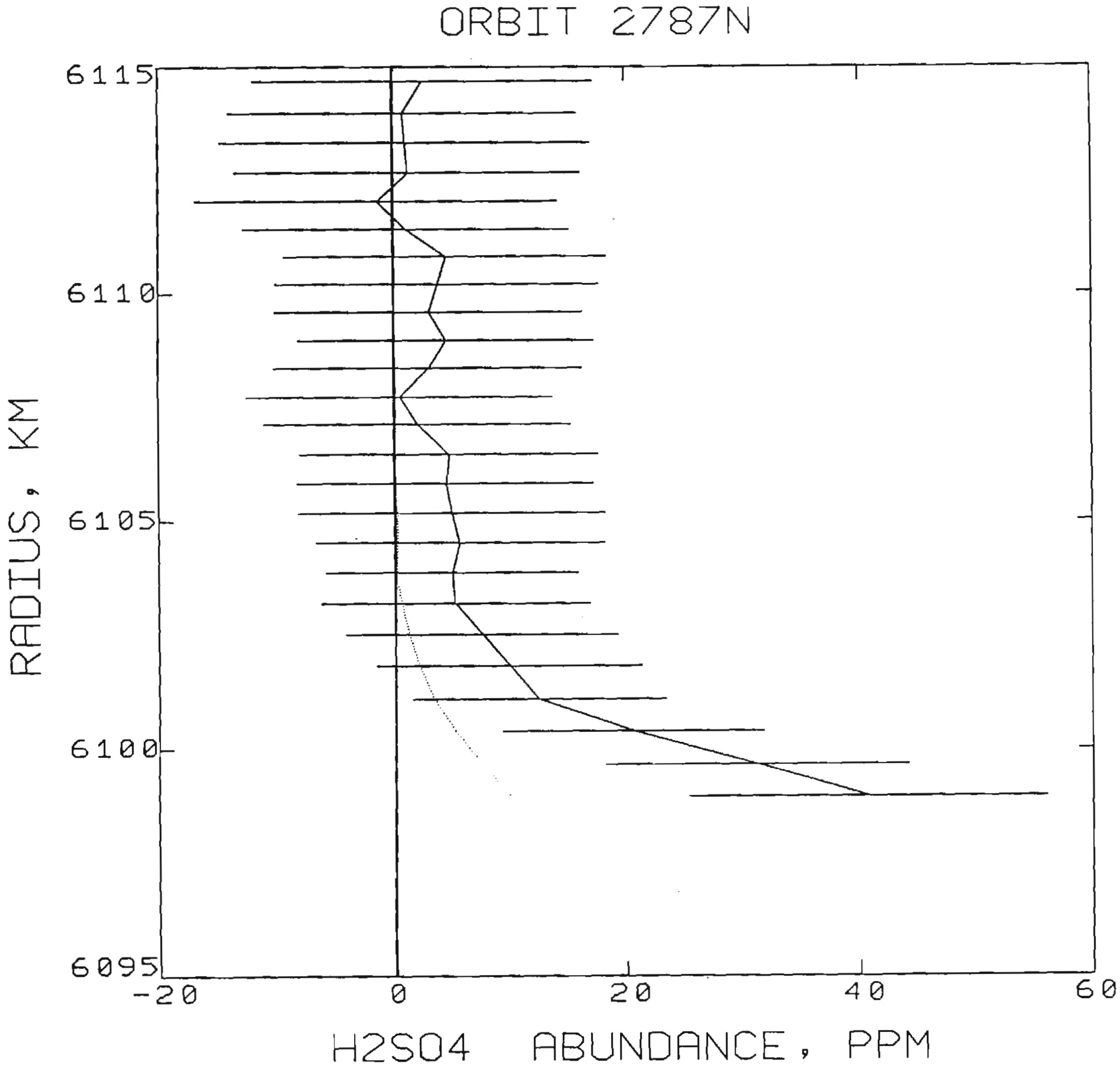

Figure 15: Sulfuric acid vapor abundance profile measured for orbit 2787N, which occurred on July 23, 1986 at 11.1°N (solid line) and the abundance expected from saturation vapor pressure (dotted line).

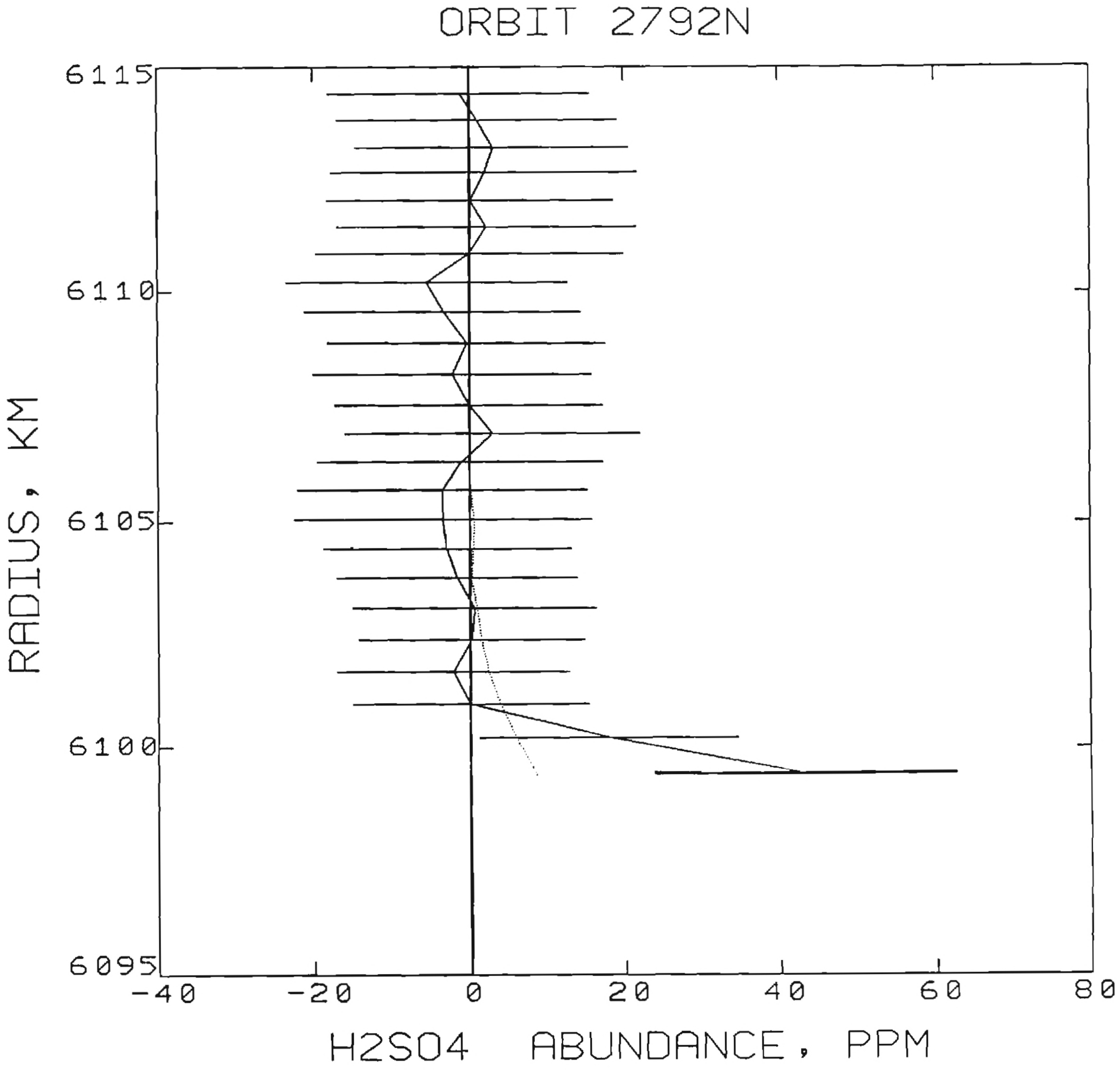

Figure 16: Gaseous H_2So_4 abundance as a function of radius measured for orbit 2792N, which occurred on July 28, 1986 at 24.8°N (solid line) and the abundance expected from saturation vapor pressure (dotted line).

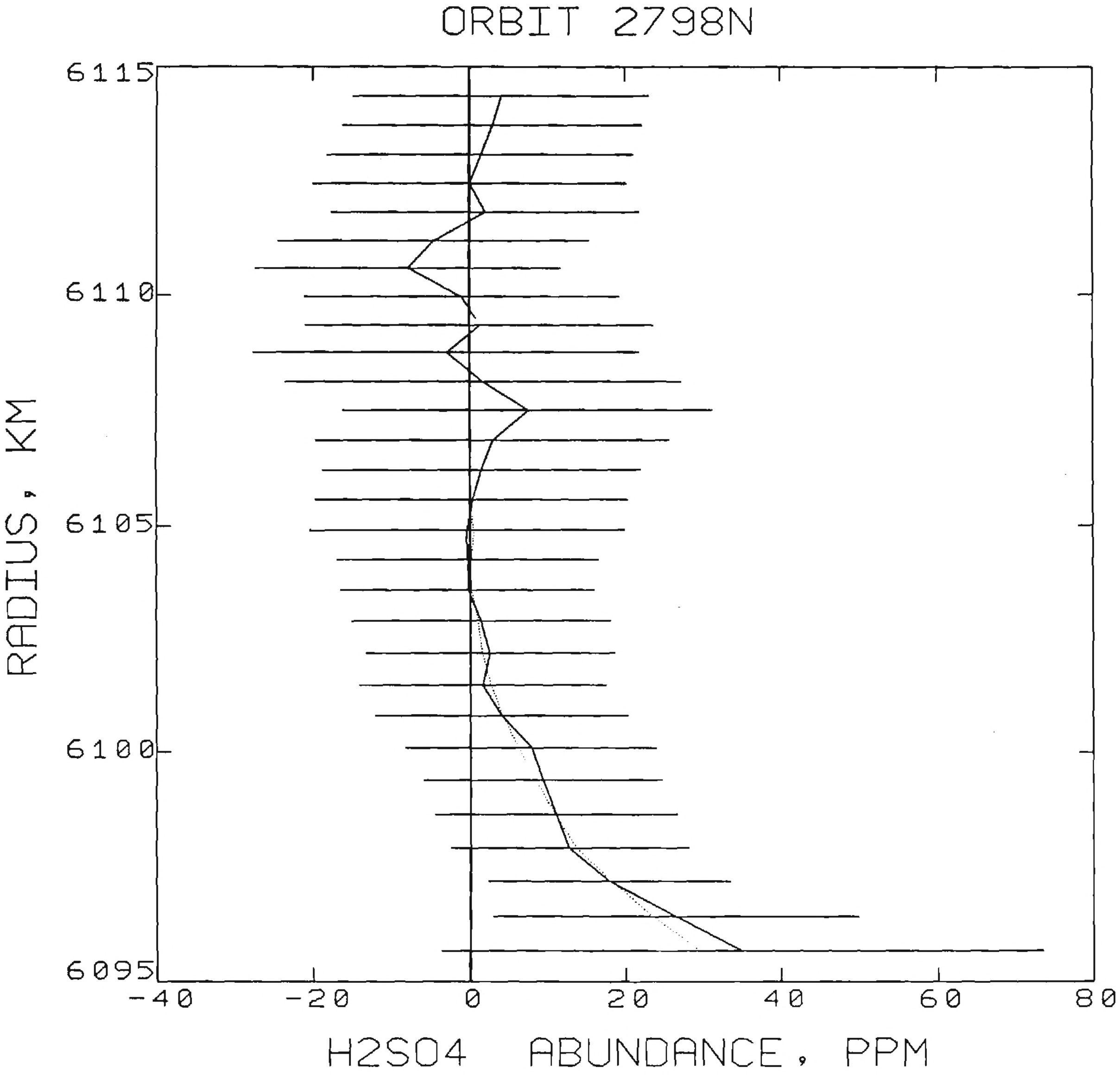

Figure 17: Sulfuric acid vapor abundance profile measured for orbit 2798N, which occurred on August 3, 1986 at 36.1°N (solid line) and the abundance expected from saturation vapor pressure (dotted line).

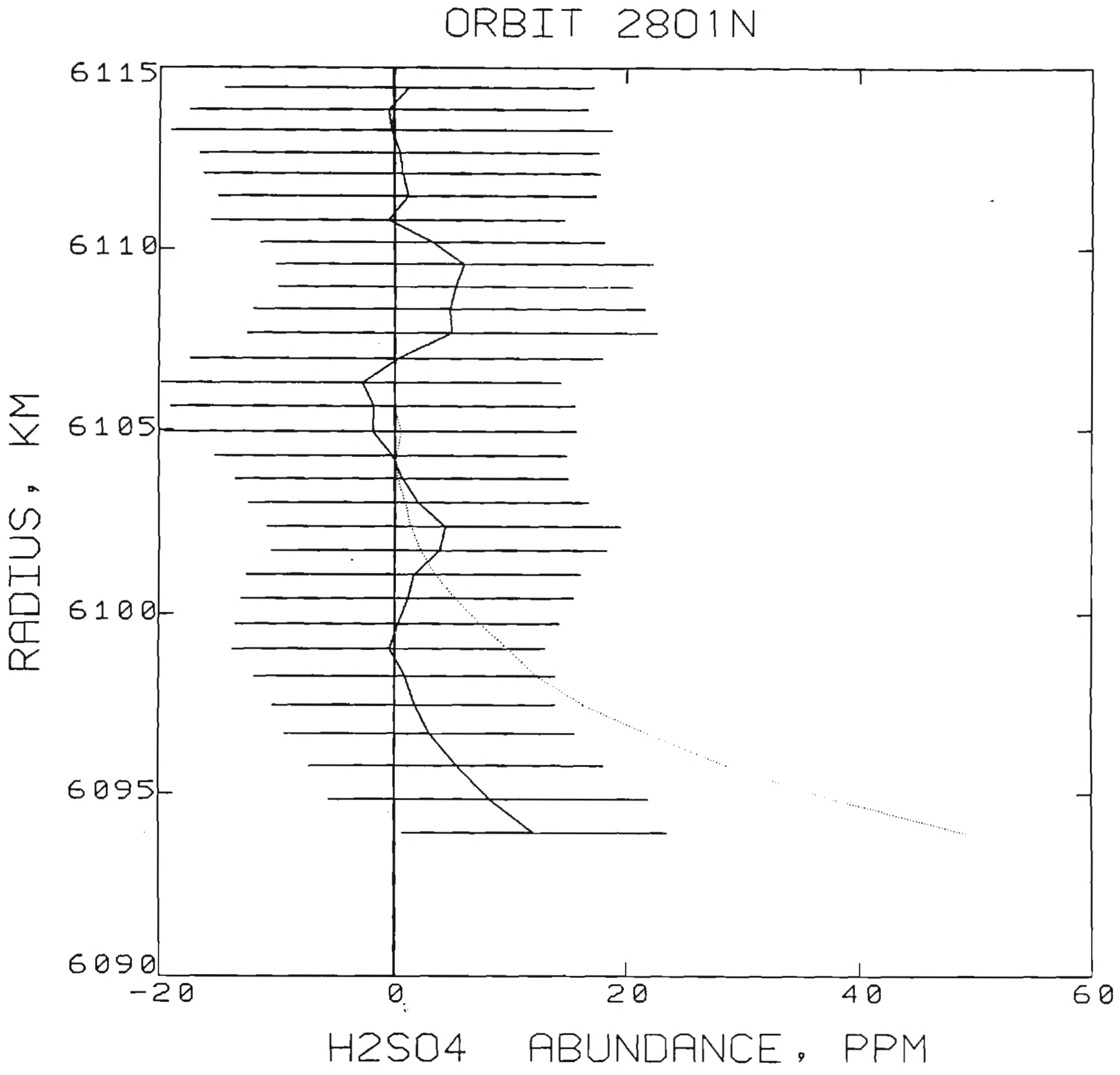

Figure 18: Gaseous H_2So_4 abundance as a function of radius measured for orbit 2801N, which occurred on August 6, 1986 at 40.8°N (solid line) and the abundance expected from saturation vapor pressure (dotted line).

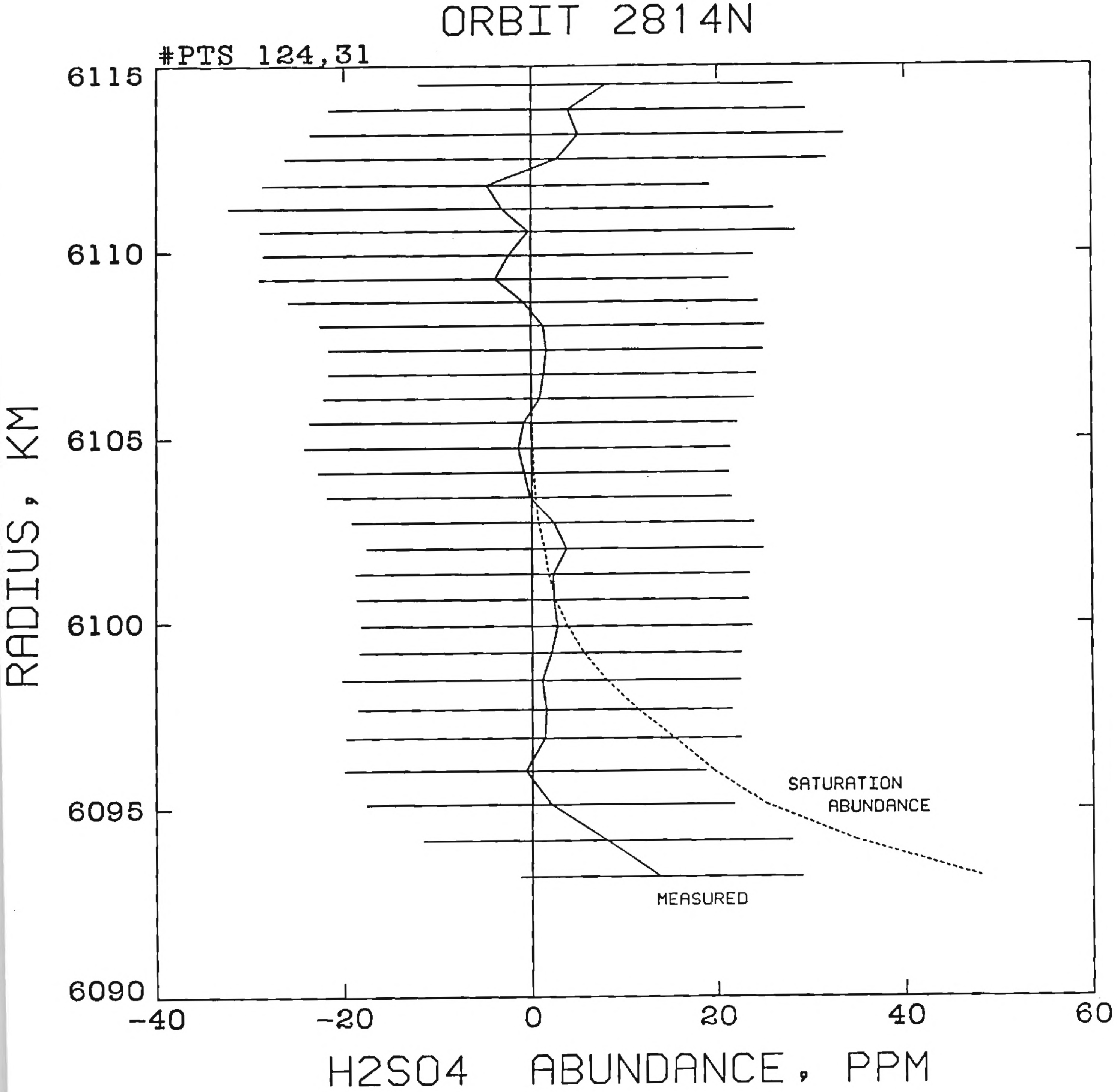

Figure 19: Sulfuric acid vapor abundance profile measured for orbit 2814N, which occurred on August 19, 1986 at 59.3°N (solid line) and the abundance expected from saturation vapor pressure (dotted line).

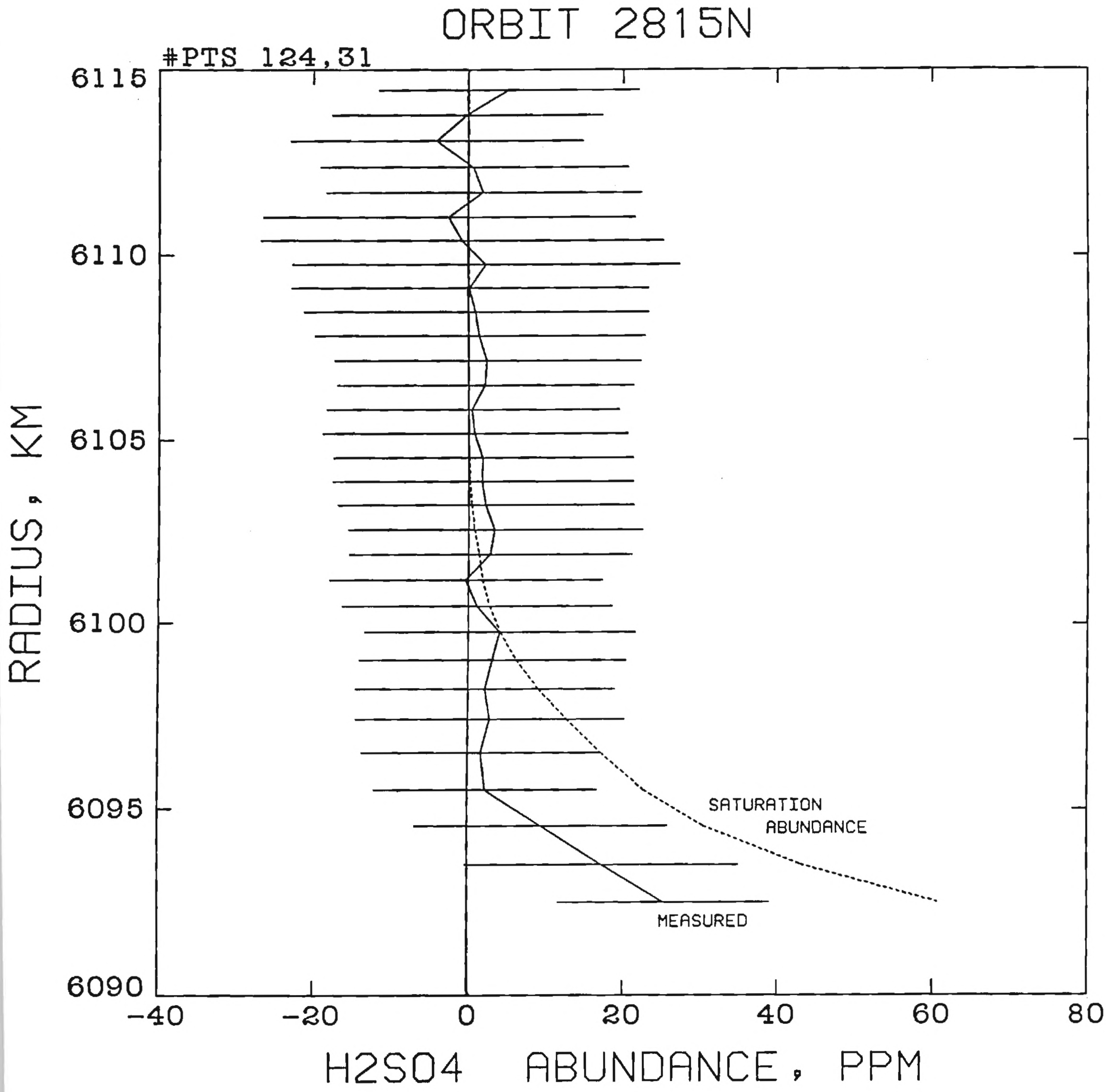

Figure 20: Gaseous H_2So_4 abundance as a function of radius measured for orbit 2815N, which occurred on August 20, 1986 at 60.7°N (solid line) and the abundance expected from saturation vapor pressure (dotted line).

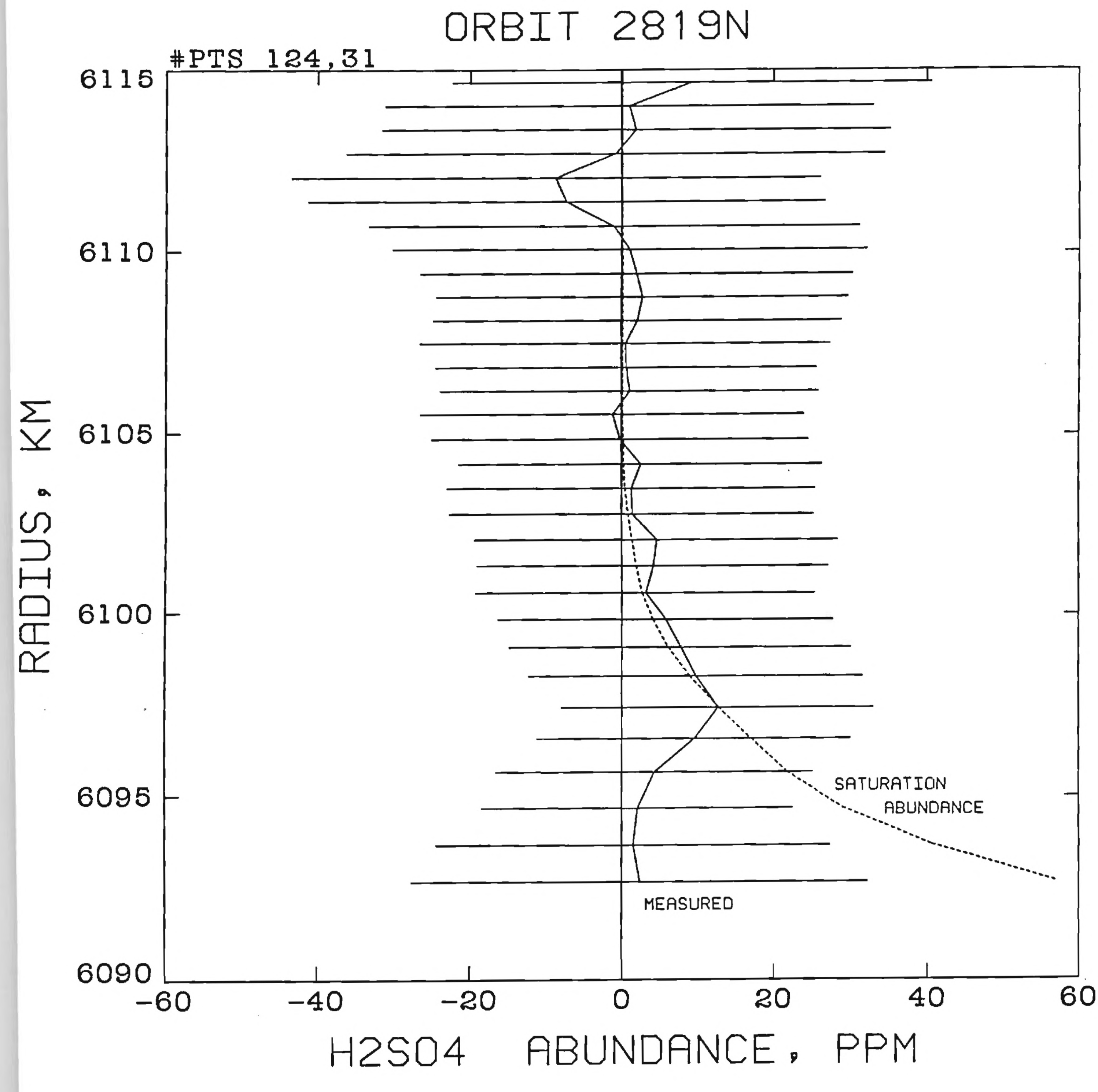

Figure 21: Sulfuric acid vapor abundance profile measured for orbit 2819N, which occurred on August 24, 1986 at 65.6°N (solid line) and the abundance expected from saturation vapor pressure (dotted line).

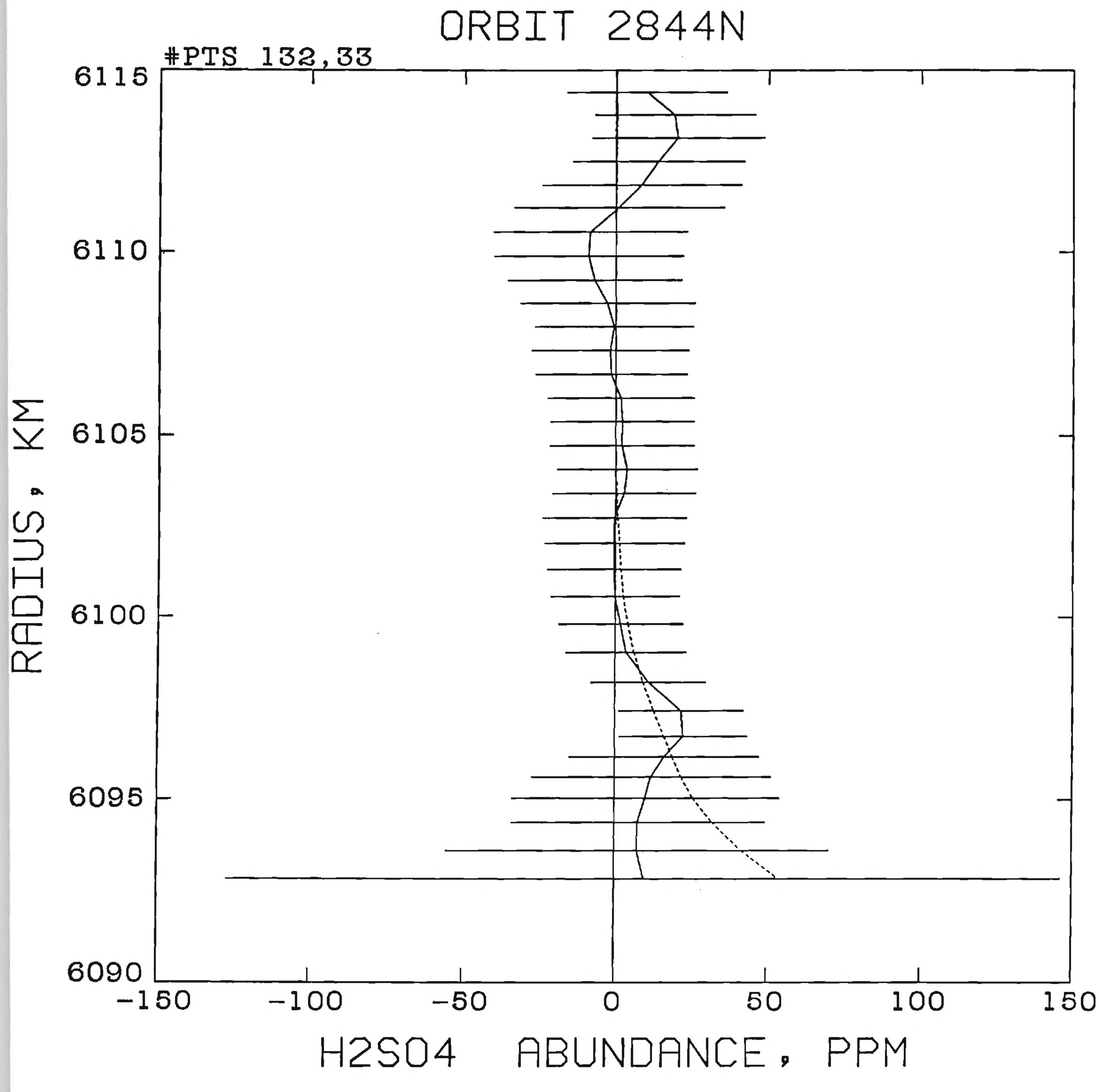

Figure 22: Gaseous H_2So_4 abundance as a function of radius measured for orbit 2844N, which occurred on September 18, 1986 at 79.6°N (solid line) and the abundance expected from saturation vapor pressure (dotted line).

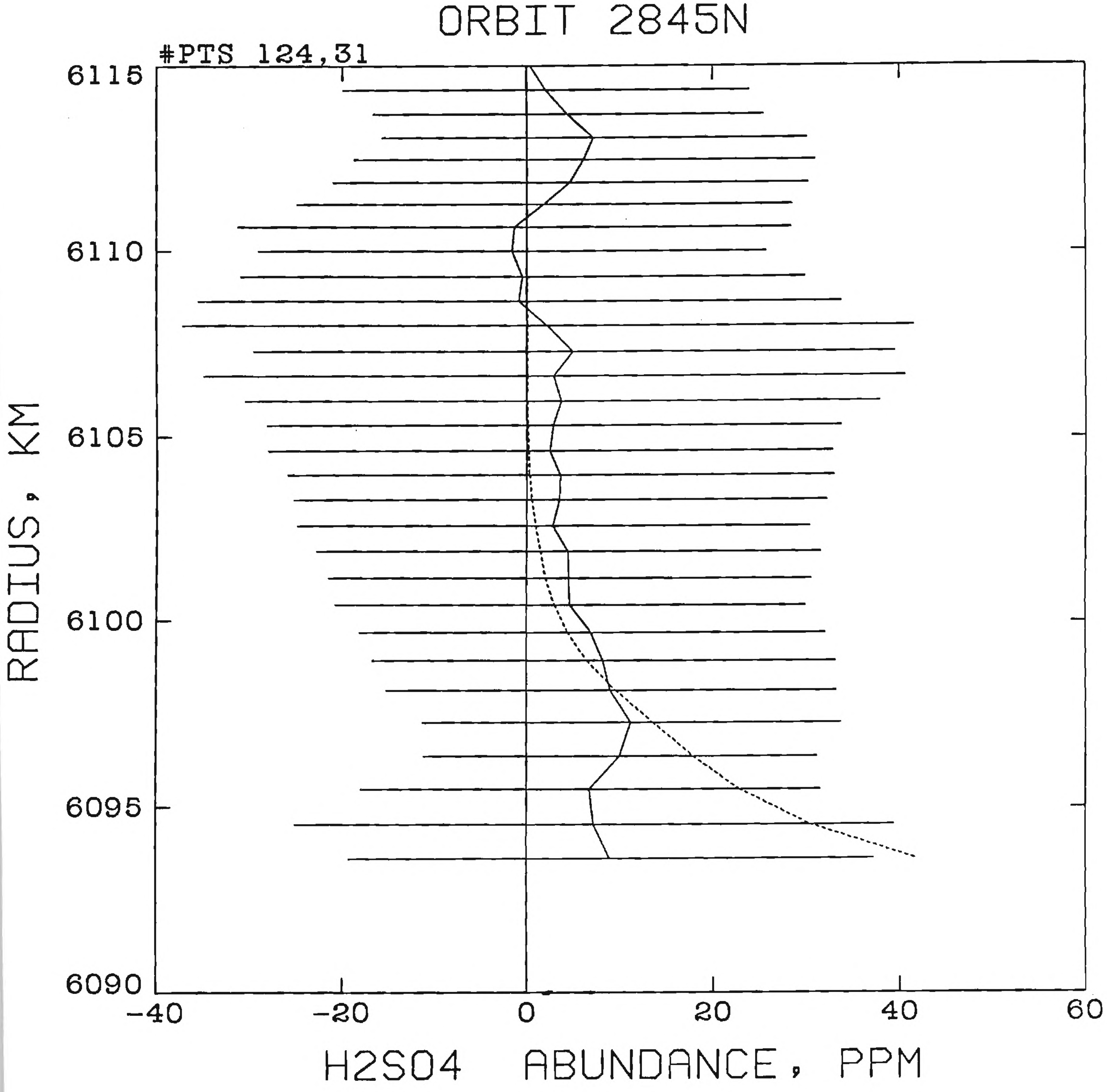

Figure 23: Sulfuric acid vapor abundance profile measured for orbit 2845N, which occurred on September 19, 1986 at 79.3°N (solid line) and the abundance expected from saturation vapor pressure (dotted line).

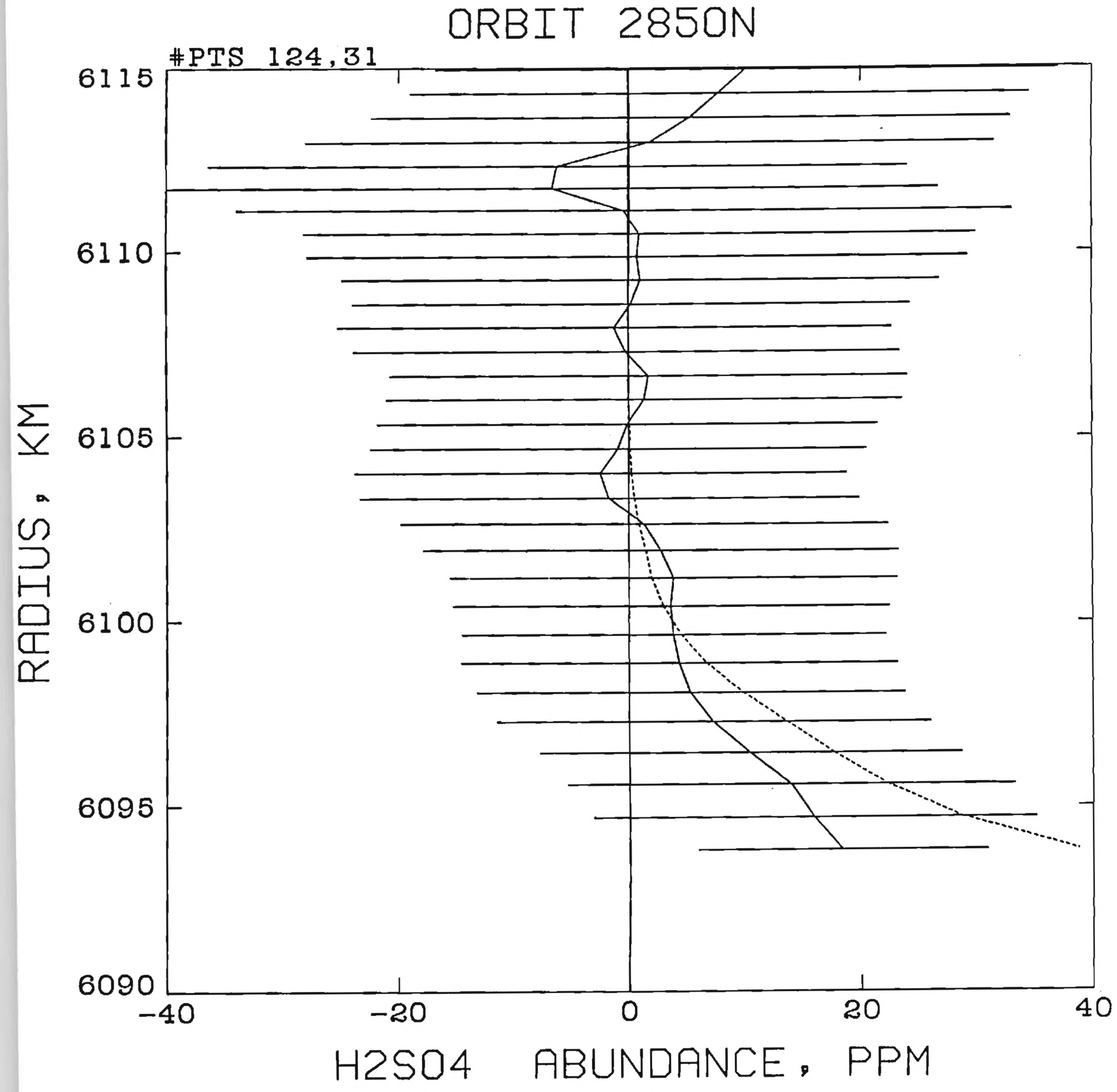

Figure 24: Gaseous H_2So_4 abundance as a function of radius measured for orbit 2850N, which occurred on September 24, 1986 at 75.6°N (solid line) and the abundance expected from saturation vapor pressure (dotted line).

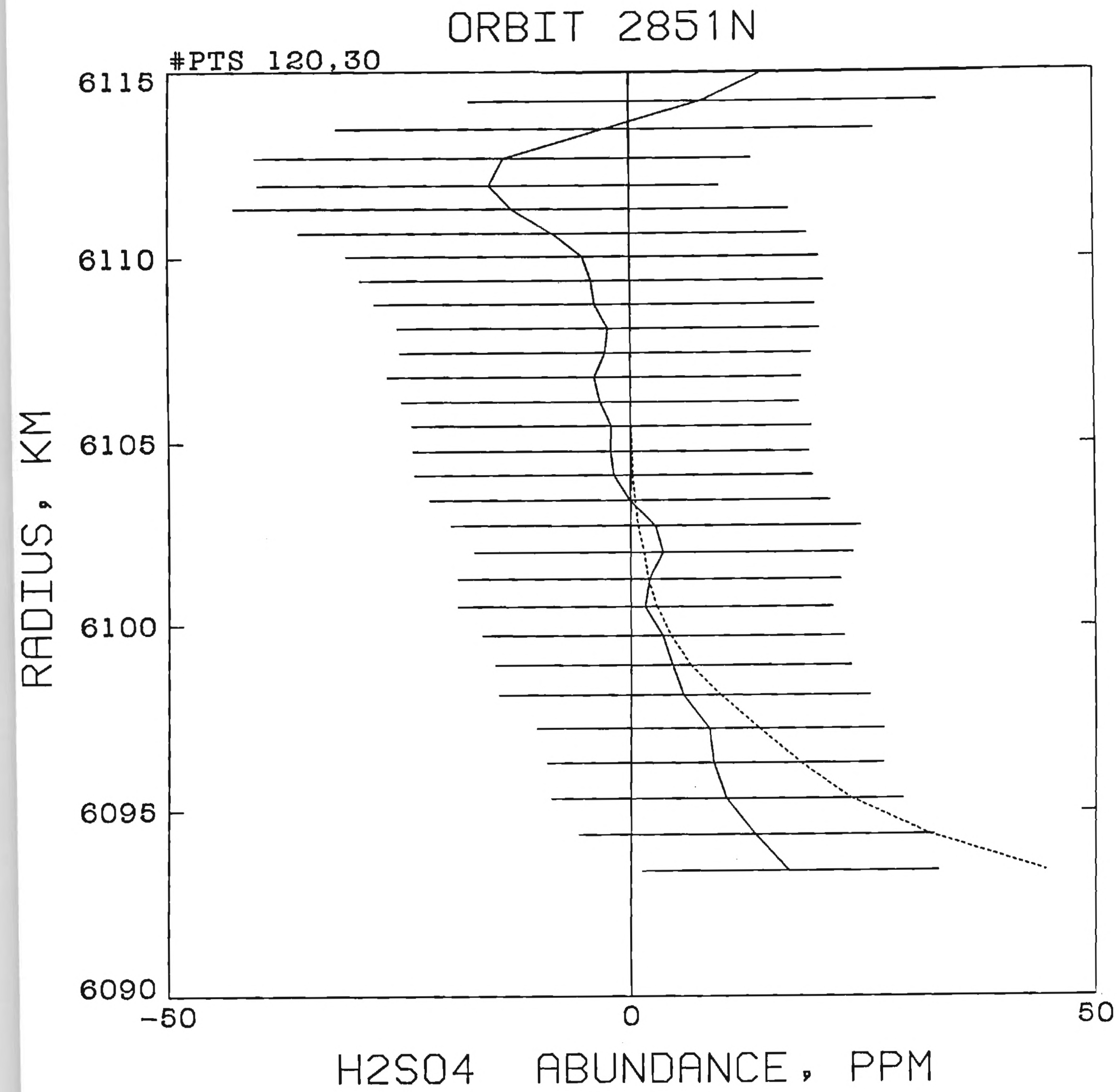

Figure 25: Sulfuric acid vapor abundance profile measured for orbit 2851N, which occurred on September 25, 1986 at 74.4°N (solid line) and the abundance expected from saturation vapor pressure (dotted line).

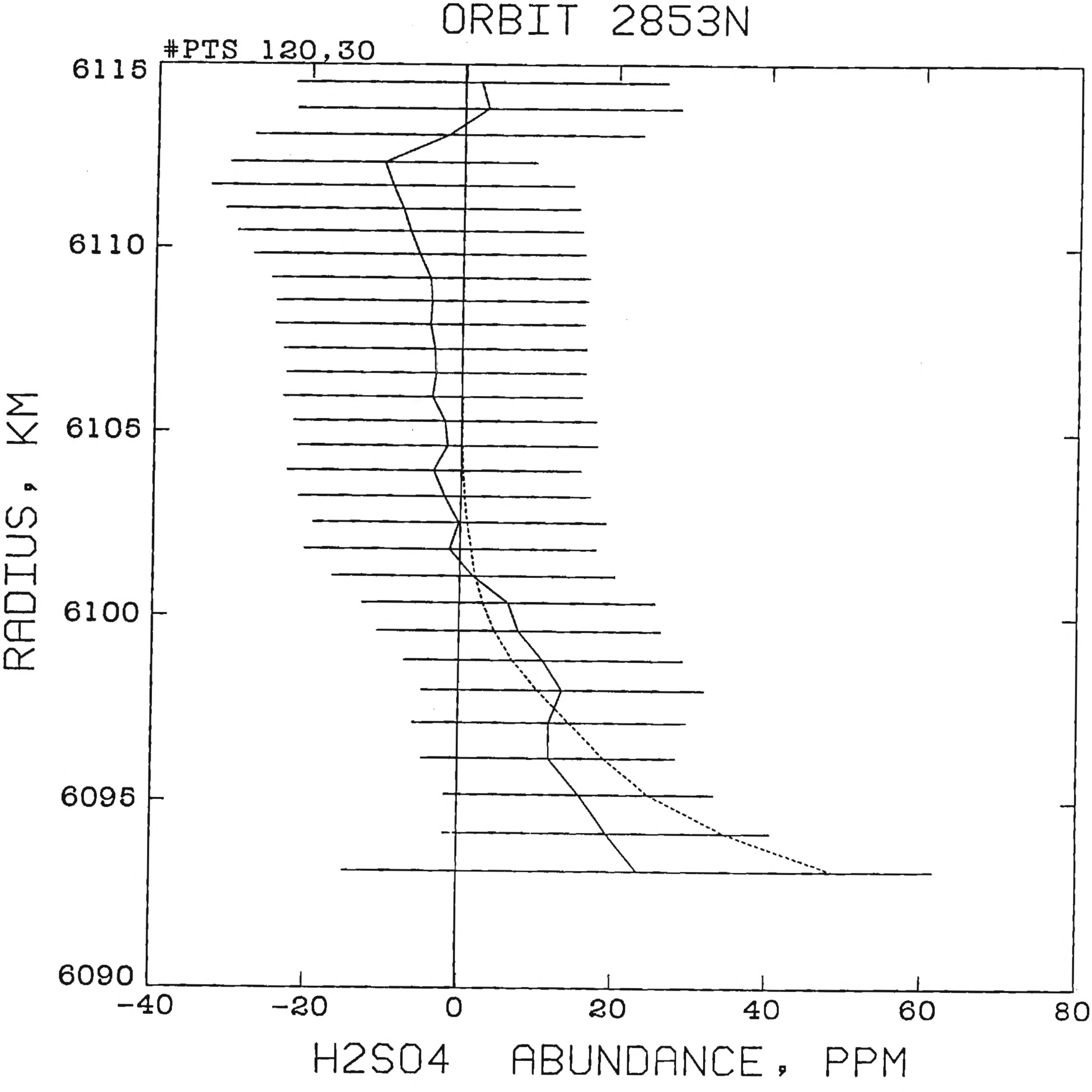

Figure 26: Gaseous H_2So_4 abundance as a function of radius measured for orbit 2853N, which occurred on September 27, 1986 at 72.6°N (solid line) and the abundance expected from saturation vapor pressure (dotted line).

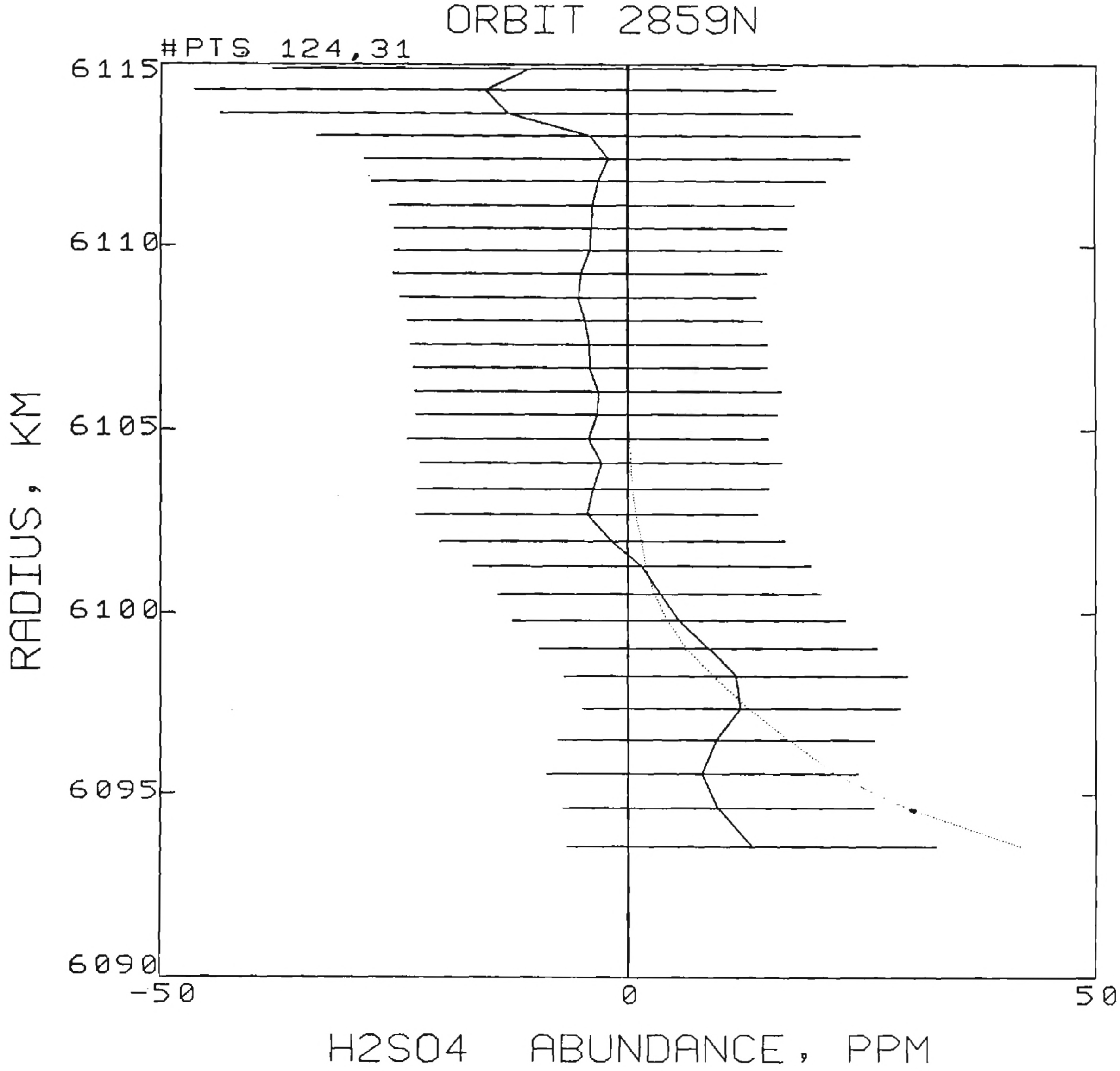

Figure 27: Sulfuric acid vapor abundance profile measured for orbit 2859N, which occurred on October 3, 1986 at 67.3°N (solid line) and the abundance expected from saturation vapor pressure (dotted line).

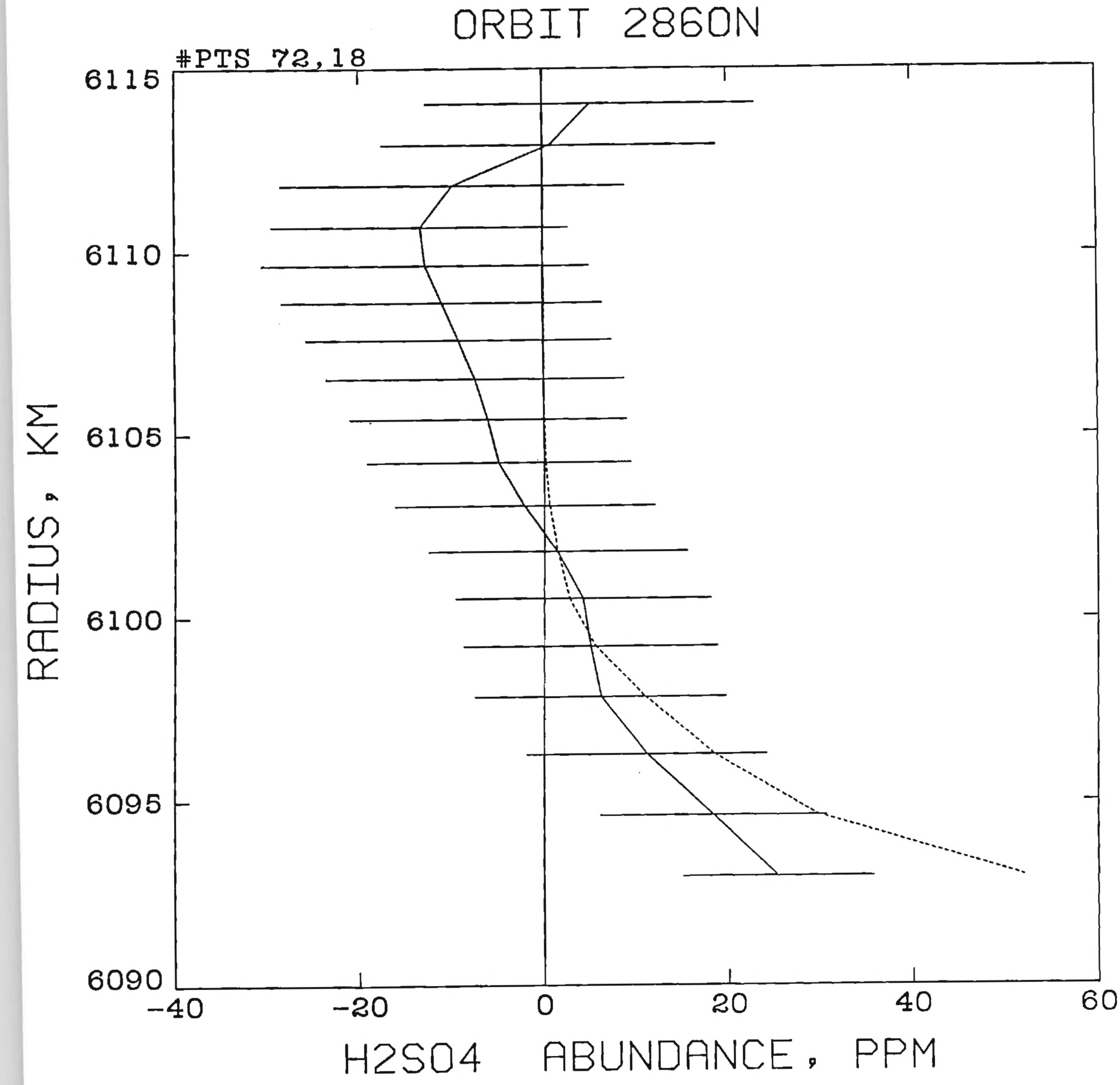

Figure 28: Gaseous H_2So_4 abundance as a function of radius measured for orbit 2860N, which occurred on October 4, 1986 at 66.7°N (solid line) and the abundance expected from saturation vapor pressure (dotted line).

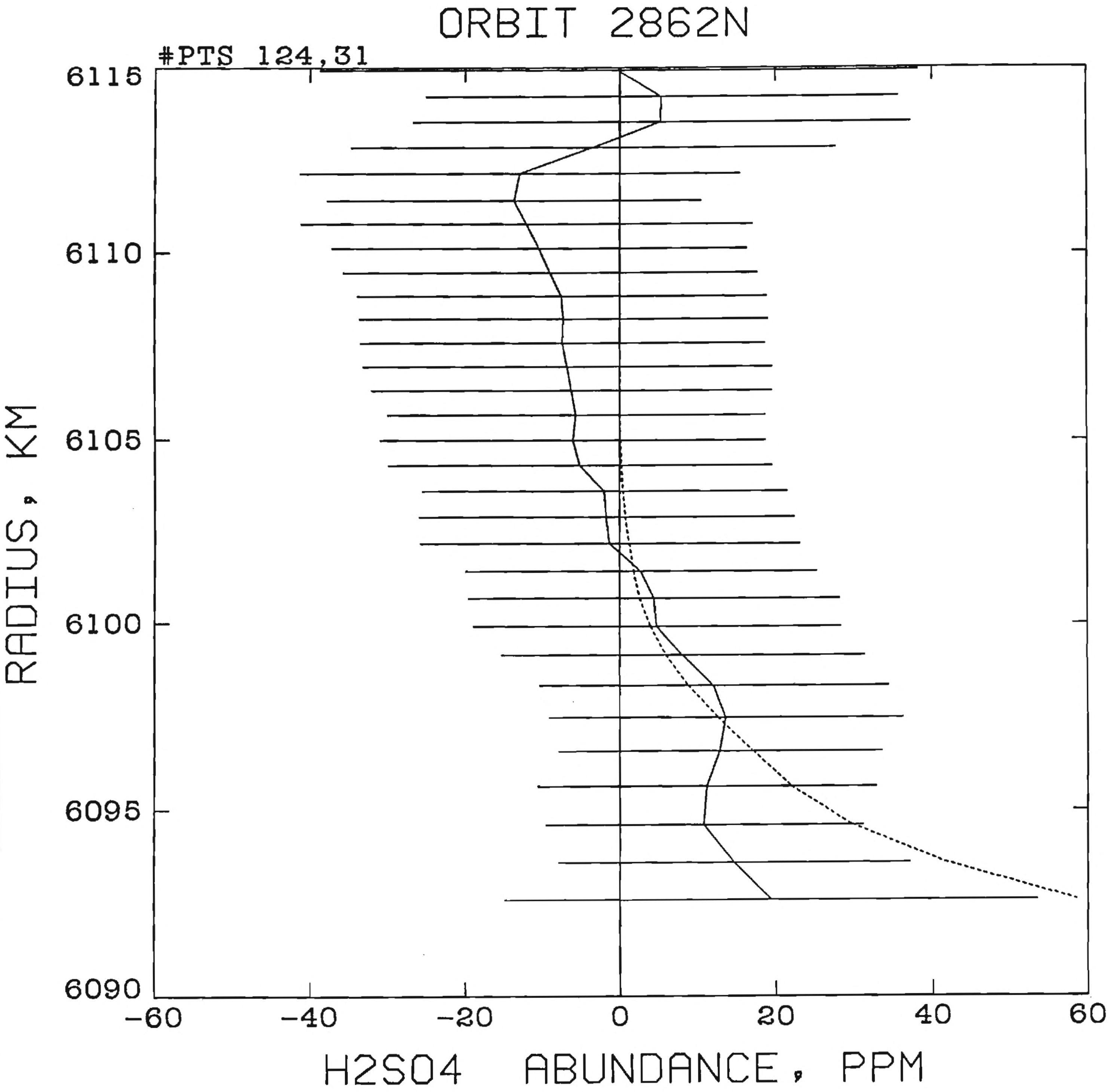

Figure 29: Sulfuric acid vapor abundance profile measured for orbit 2862N, which occurred on October 6, 1986 at 65.9°N (solid line) and the abundance expected from saturation vapor pressure (dotted line).

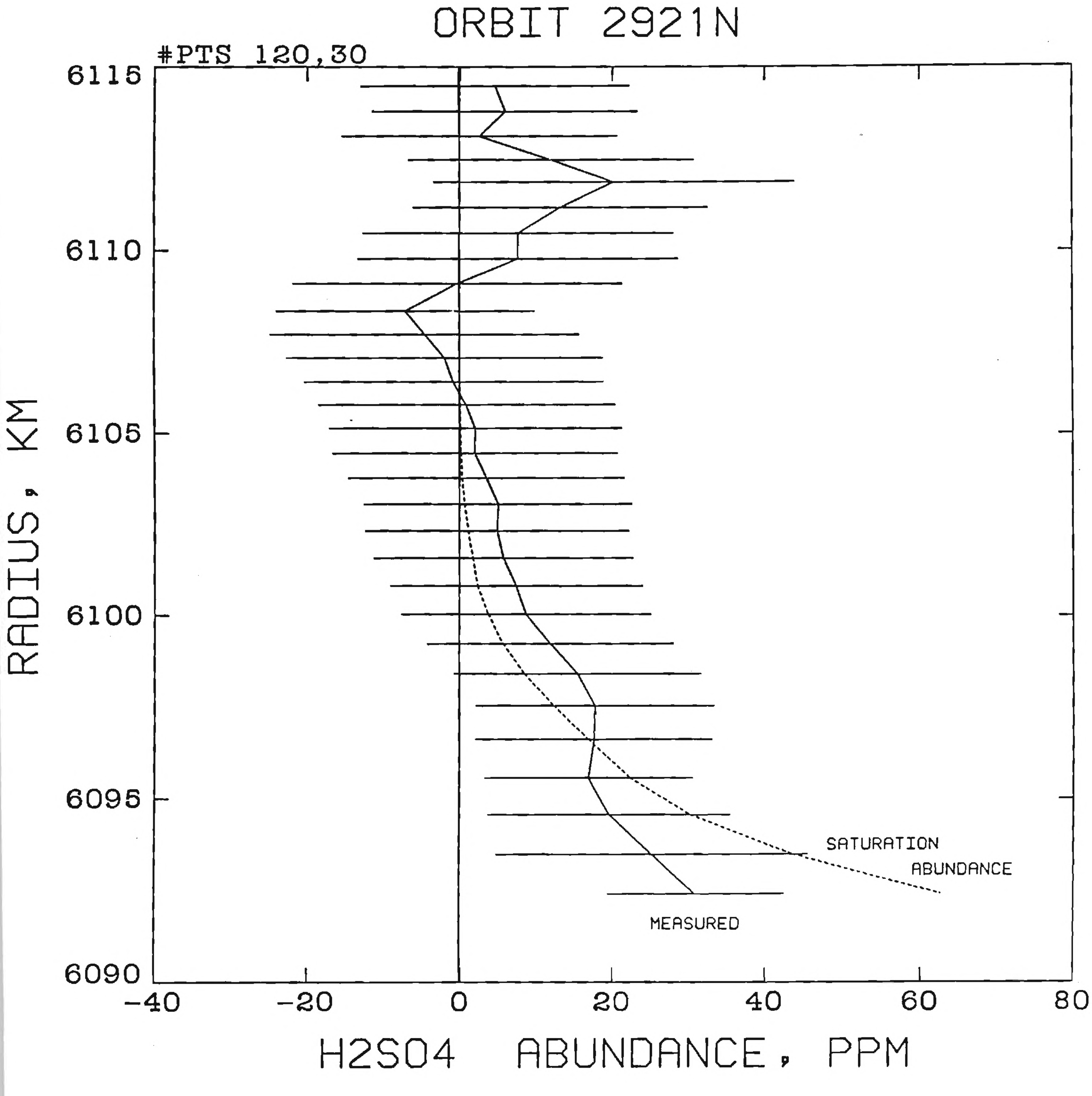

Figure 30: Gaseous H_2So_4 abundance as a function of radius measured for orbit 2921N, which occurred on December 4, 1986 at 87.2°N (solid line) and the abundance expected from saturation vapor pressure (dotted line).

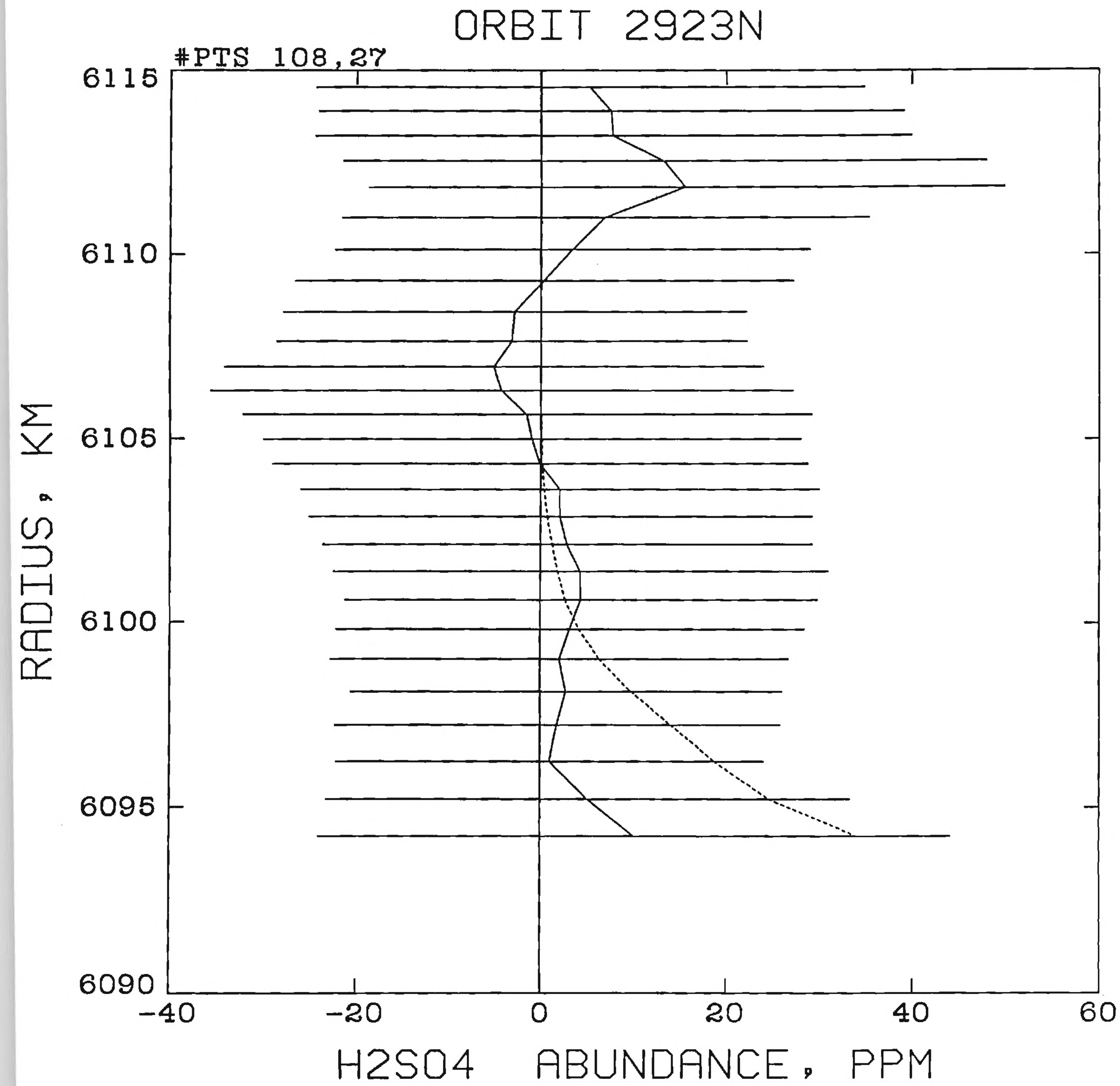

Figure 31: Sulfuric acid vapor abundance profile measured for orbit 2923N, which occurred on December 6, 1986 at 88.0°N (solid line) and the abundance expected from saturation vapor pressure (dotted line).

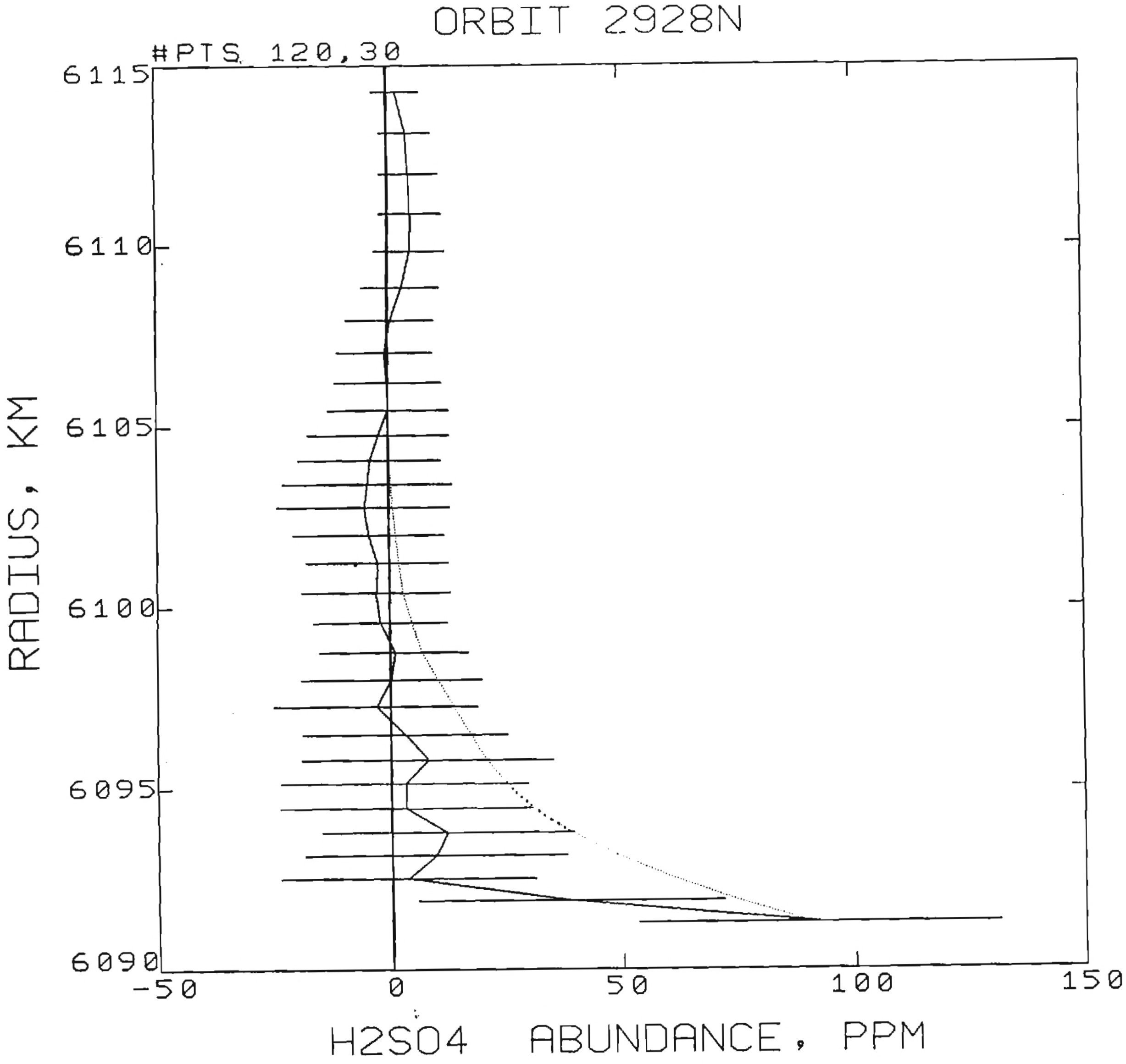

Figure 32: Gaseous H_2So_4 abundance as a function of radius measured for orbit 2928N, which occurred on December 11, 1986 at 88.6°N (solid line) and the abundance expected from saturation vapor pressure (dotted line).

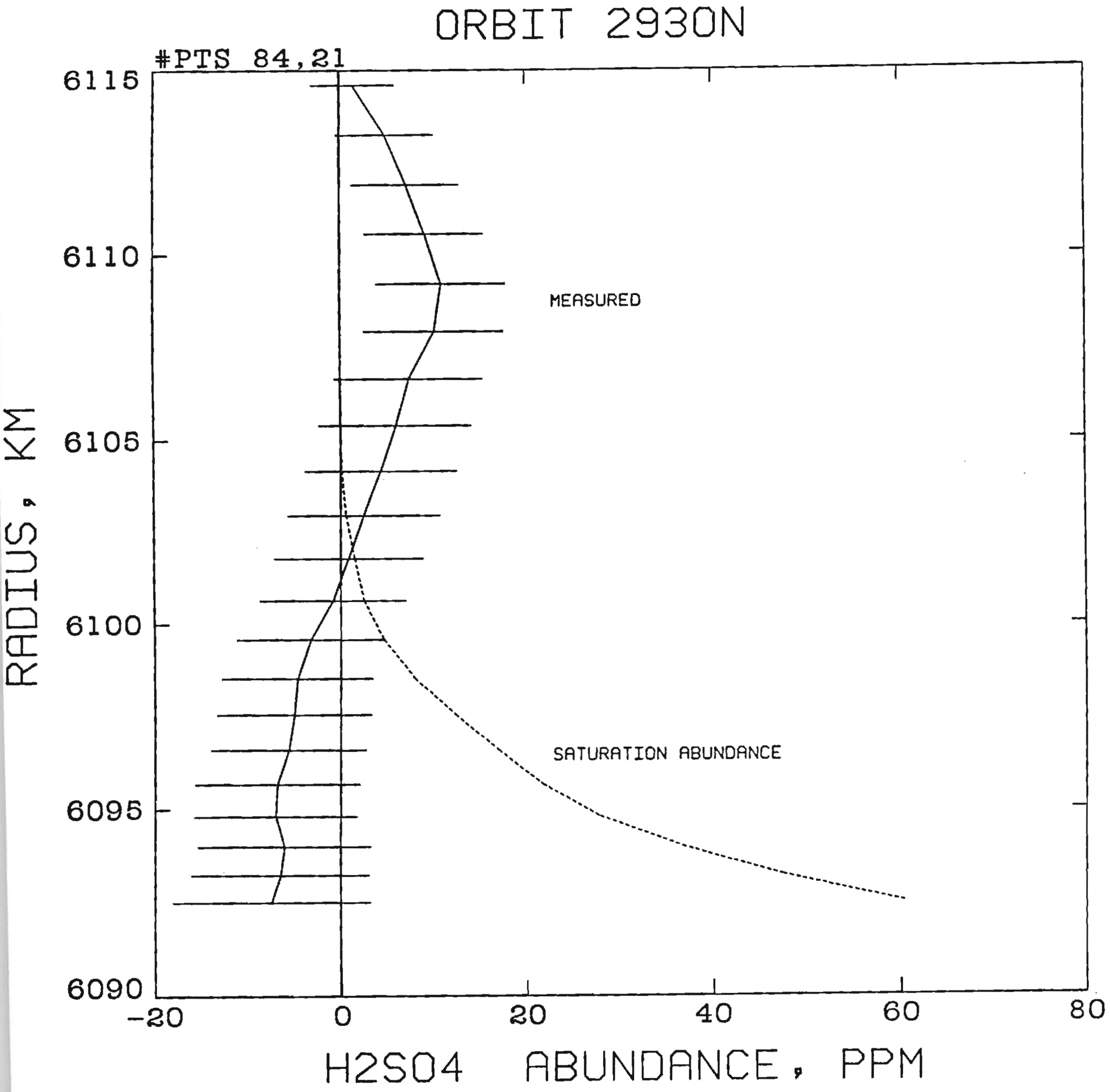

Figure 33: Sulfuric acid vapor abundance profile measured for orbit 2930N, which occurred on December 13, 1986 at 87.5°N (solid line) and the abundance expected from saturation vapor pressure (dotted line).

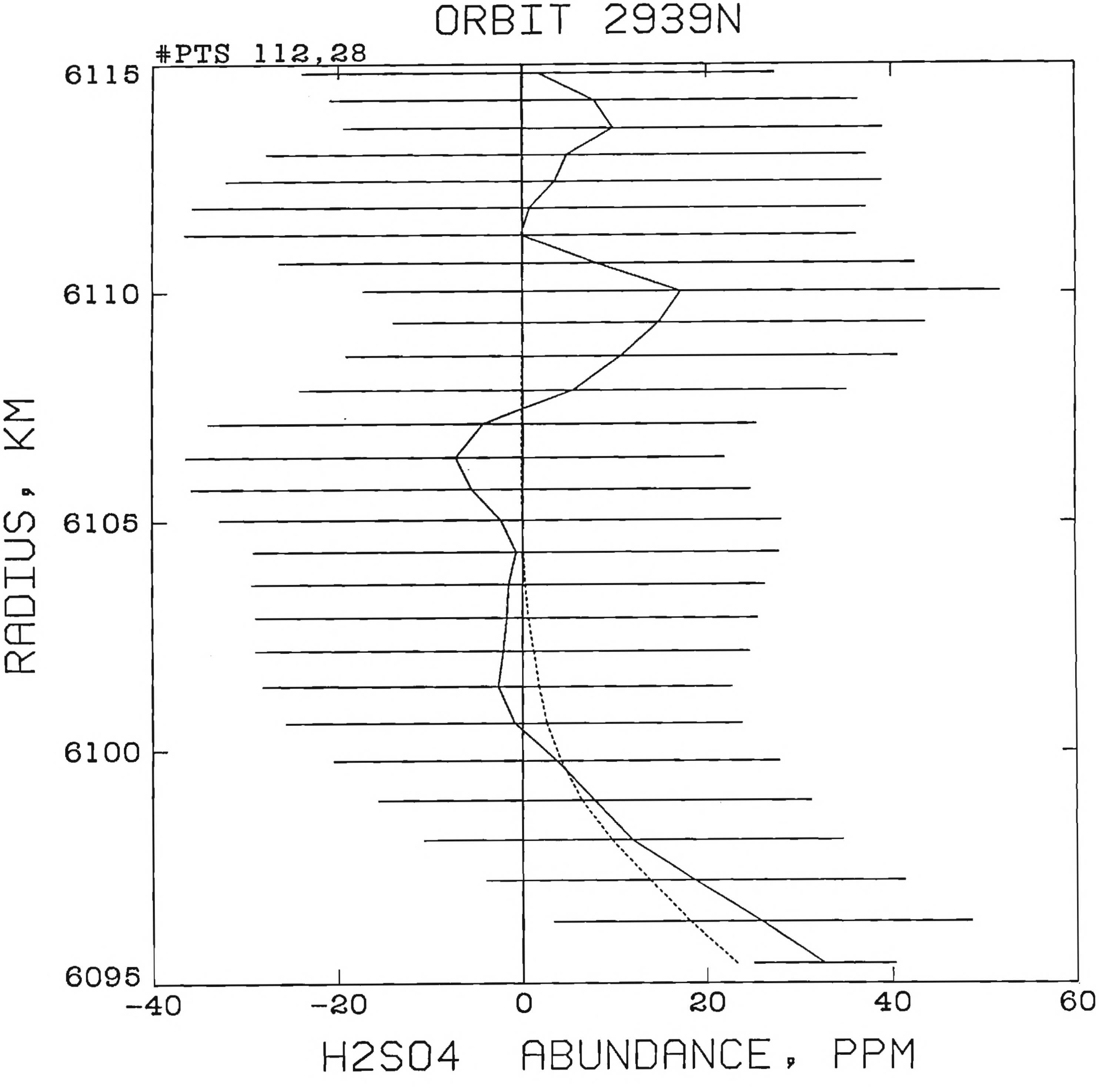

Figure 34: Sulfuric acid vapor abundance profile measured for orbit 2939N, which occurred on December 22, 1986 at 77.8°N (solid line) and the abundance expected from saturation vapor pressure (dotted line).

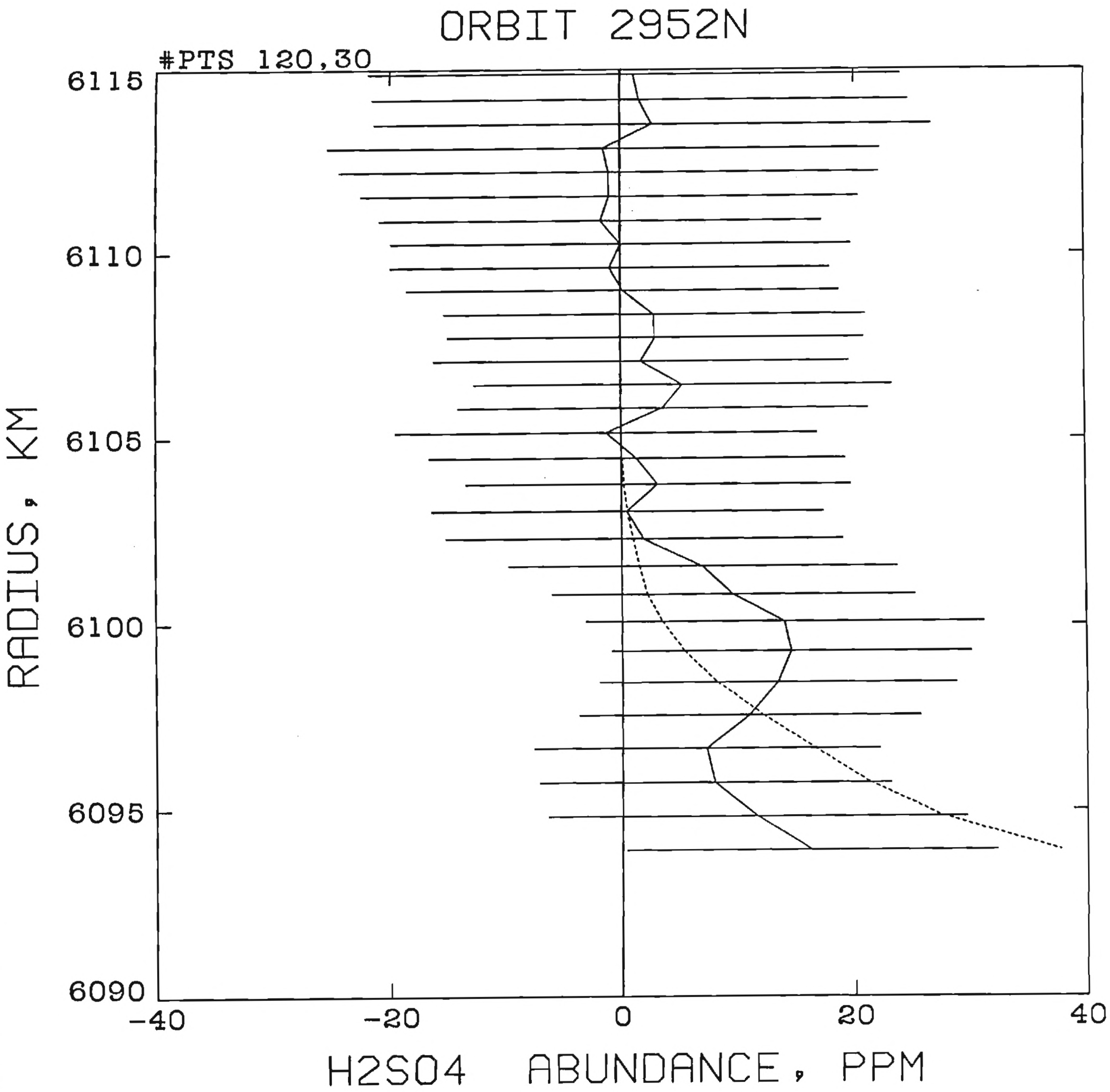

Figure 35: Gaseous H_2So_4 abundance as a function of radius measured for orbit 2952N, which occurred on January 4, 1986 at 60.4°N (solid line) and the abundance expected from saturation vapor pressure (dotted line).

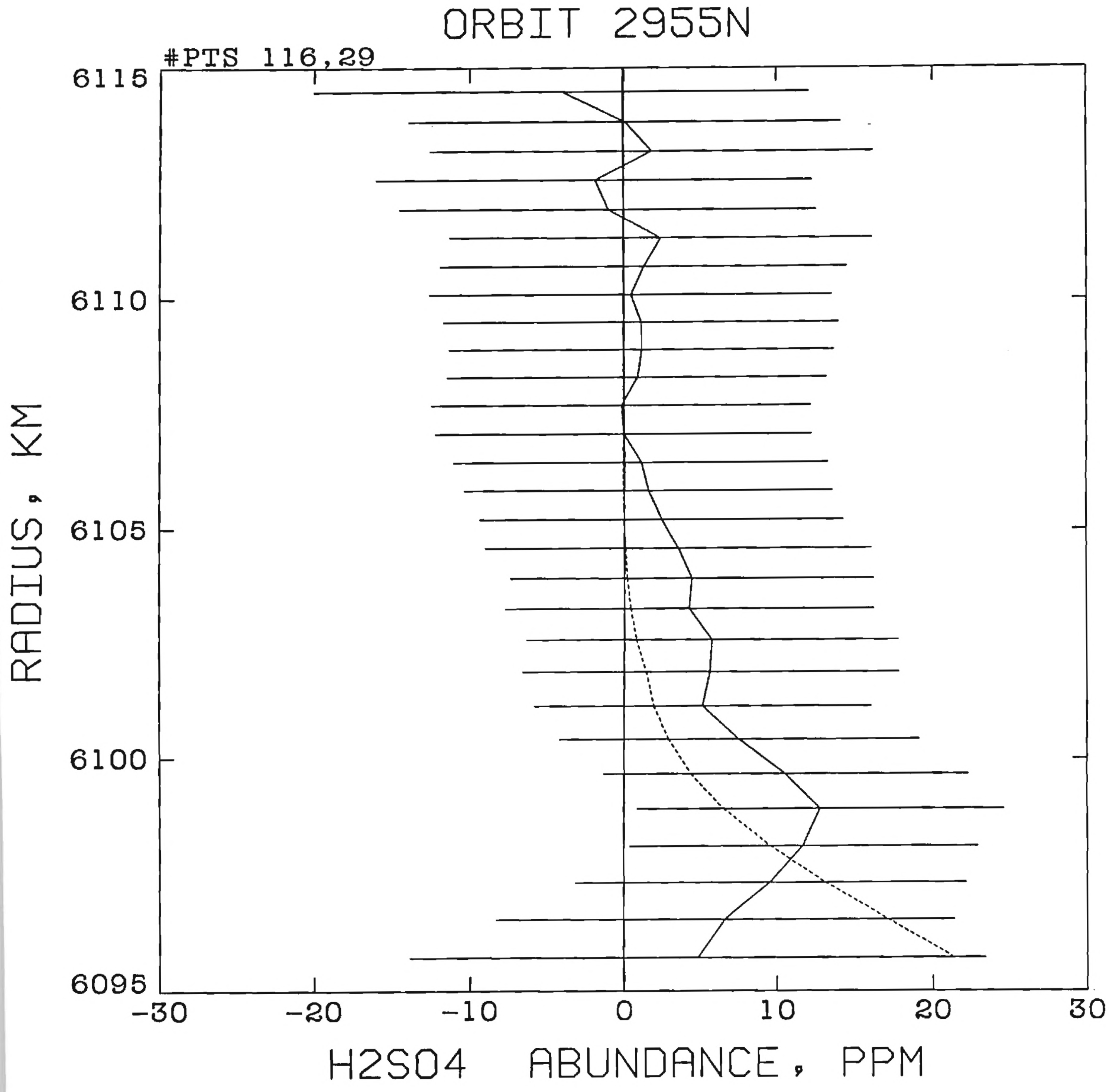

Figure 36: Sulfuric acid vapor abundance profile measured for orbit 2955N, which occurred on January 7, 1986 at 56.4°N (solid line) and the abundance expected from saturation vapor pressure (dotted line).